Simulated Dispersion Measures of the Intergalactic Medium

A dissertation submitted to the University of Manchester for the degree of Master of Science by Research in the Faculty of Science and Engineering

2021

By

Henry R Adams

School of Physics and Astronomy

Contents

Word count: 17219

List of Tables

List of Figures

Abstract

ABSTRACT OF DISSERTATION submitted by Henry R Adams
for the Degree of Master of Science by Research and entitled
Simulated Dispersion Measures of the Intergalactic Medium
September 2021

Fast radio bursts (FRBs) can be observed by their large dispersion in time across the different frequencies from which they are made. This dispersion measure (DM) depends on the number of electrons along its path. This allows them to act as a cosmological probe for gas in the intergalactic medium (IGM) and may be used to investigate the missing baryon problem, in which a discrepancy between the predicted and observed baryon densities have been found. We have used the Evolution and Assembly of GaLaxies and their Environments (EAGLE) simulation to simulate the DM from FRBs using a box stacking method and find the mean DM - z relation to follow the cosmological average. We found the scatter of the result to be significantly non Gaussian, being better represented by a log-normal distribution and that observations broadly agree with the results. We also examined the effect of host haloes by setting sight lines to start at the centre of haloes of different mass. We find that haloes play a significant role in the DM at lower redshifts but become less important at larger distances. Finally we examined the contributions from different gas overdensities of the IGM and found the overdense group contributes the most to the DM, and that the DM contribution drops off significantly with increasing overdensity.

Declaration

No portion of the work referred to in this dissertation has been submitted in support of an application for another degree or qualification of this or any other university or other institution of learning.

Copyright

Acknowledgements

Thanks to Professor Scott Kay for his guidance throughout this research project and from whom, despite having never met in person, I have learnt much.

The Author

Originally from Coventry, the author obtained a BSc with honours in Physics from the University of Warwick in 2020. This thesis represents the author's time as a MScR student at the Jodrell Bank Center for Astrophysics, working with Professor Scott Kay.

Chapter 1

Introduction

The Λ Cold Dark Matter model (ΛCDM) has been used to predict the make-up of the Universe, its dark energy, radiation and matter densities. The evolution of these densities have been tracked throughout the Universe's history, backed up by observations from measurements of the Cosmic Microwave Background (CMB), weak/strong lensing, galaxy surveys and supernovae (Komatsu et al. 2011; Planck Collaboration et al. 2020a; Riess et al. 2004; Dey et al. 2019). In more recent times, from redshift $z = 0$ up until $z \approx 1$, a significant amount of the baryonic matter is unaccounted for. This has been called the missing baryon problem. A number of methods have been used to attempt to locate these missing baryons including the use of the Sunyaev-Zel'dovich effect, improved direct x-ray observations and measuring Dispersion Measures (DM) from fast radio bursts (FRBs) (Birkinshaw 1999; Perna and Loeb 1998; Petroff et al. 2019).

1.1 Cosmology

To understand how these methods work, how the missing baryon problem has arisen and the wider context of the Universe, an overview of cosmology is required and outlined in this section. Einstein's theory of general relativity describes the nature of how gravity influences universes. The accepted solution that describes

the Universe we observe is given by the Friedmann-Lemaitre-Robertson-Walker (FLRW), metric which assumes, on large scales, a homogeneous and isotropic universe

$$ds^2 = dt^2 - a^2(t)\left[\frac{dr^2}{1-kr^2} + r^2(d\theta^2 + \sin^2\theta d\phi^2)\right]. \tag{1.1}$$

The equation is given in spherical coordinates and natural units ($c = 1$), with k the constant curvature, r, a dimensionless radius that varies with curvature and a, the scale factor, which is given by

$$a(t) = \frac{1}{1+z(t)}, \tag{1.2}$$

with $z(t)$ the redshift. By using the Einstein equation and the assumptions of a homogeneous and isotropic universe, one of the Friedmann equations can be found

$$H^2 = H_0^2\left(\frac{\Omega_{m,0}}{a^3} + \frac{\Omega_{r,0}}{a^4} + \Omega_{\Lambda,0} + \frac{\Omega_{k,0}}{a^2}\right), \tag{1.3}$$

with H the Hubble parameter which is defined by $\dot{a}(t)/a(t)$ and $\Omega_{m,0}, \Omega_{r,0}, \Omega_{\Lambda,0}, \Omega_{k,0}$ the present day values of the density parameters of matter, radiation, dark energy, curvature given by

$$\Omega \equiv \frac{\rho(t_0)}{\rho_c(t_0)}, \qquad \rho_c = \frac{3H^2}{8\pi G}, \tag{1.4}$$

with ρ_c the critical density of the universe and t_0 the time for the present day. The Friedmann equation shows how the relative importance of all the components of the universe changes over time. Initially the Universe was dominated by radiation, then matter and now dark energy. The current accepted values for the density parameters, and the ones used in this thesis, have been found from measurements of the CMB taken by the Planck satellite and are shown in Table 1.1.

The ΛCDM model was built on a Friedmann universe and is the simplest

Density	Planck18 value
$\Omega_{m,0}h^2$	0.1430 ± 0.0011
$\Omega_{c,0}h^2$	0.1200 ± 0.0012
$\Omega_{b,0}h^2$	0.02237 ± 0.00015
$\Omega_{k,0}$	0.0007 ± 0.0019
$\Omega_{\Lambda,0}$	0.6847 ± 0.0073

Table 1.1: The values of the densities from the Planck satellite with $\Omega_{c,0}$ the dark matter density and h the dimensionless hubble parameter, $h = 0.677$ given by $H_0/[100(\text{km/s})/\text{Mpc}]$, (Planck Collaboration et al. 2020b).

model that predicts structure, the existence of the CMB and the accelerating expansion of the Universe. It assumes that dark matter is cold (non-relativistic), collisionless (only interacts with gravity) and does not release energy via photon radiation (retains energy as kinetic or gravitational potential energy).

1.2 Structure Formation

1.2.1 Linear Theory

A continuation from cosmology is how inhomogeneities in matter within the Universe evolve over time. The very early Universe was near homogeneous with quantum fluctuations that were magnified by inflation. The over/underdensity of a region is given by

$$\delta(\mathbf{x}, t) = \frac{\rho(\mathbf{x}, t) - \rho_b(t)}{\rho_b(t)}, \tag{1.5}$$

with $\rho_b(t)$ the background density and $\mathbf{x}$ the comoving (scaled for the expansion of the Universe) position vector such that $\mathbf{r} = a(t)\mathbf{x}$. δ ranges from -1 to ∞ with underdense regions given by, $-1 < \delta < 0$ and overdense regions, $\delta > 0$. The early Universe was made up of only small fluctuations which is the same as an overdensity of $\delta \ll 1$ everywhere. The evolution of the density fluctuations can be modelled linearly in the early stages assuming: fluctuations are small;

flow is coherent (i.e. pressure is negligible); gravity is a weak field (can use Newtonian gravity); and the effects of baryons are negligible. The background solution (no perturbations) for velocity, density and potential, can be derived from the continuity, Euler and Poisson equations for a collisionless fluid

$$v_b = \dot{a}x = Hr, \tag{1.6}$$

$$\rho_b(a) = \frac{\rho_{b,0}}{a^3}, \tag{1.7}$$

$$\phi_b = \frac{2}{3}\pi G\rho_b r^2, \tag{1.8}$$

where the dot indicates a time derivative. A solution for small fluctuations can then be written as

$$v = v_b + \delta v, \tag{1.9}$$

$$\rho = \rho_b(1+\delta), \tag{1.10}$$

$$\phi = \phi_b + \delta\phi. \tag{1.11}$$

Inserting these into the continuity, Euler and Poisson equations and discarding the products of the perturbed terms as they are small (approximating to first order) leaves the linearised forms of the continuity, Euler and Poisson equations

$$\frac{d\delta}{dt} + \nabla_x \cdot \dot{\mathbf{x}} = 0, \tag{1.12}$$

$$\frac{d\dot{\mathbf{x}}}{dt} + 2H\dot{x} + \frac{1}{a^2}\nabla_x\delta\phi = 0, \tag{1.13}$$

$$\nabla_x^2\delta\phi - 4\pi G\rho_b a^2\delta = 0, \tag{1.14}$$

which are valid for $\delta \ll 1$ with $\nabla_x = a\nabla$, the comoving gradient operator, G,

Newton's gravitational constant and $d\delta/dt$, the connective derivative for fixed observers in comoving coordinates given by

$$\frac{d\delta}{dt} = \frac{\partial\delta}{\partial t} + (v_b \cdot \nabla)\delta. \tag{1.15}$$

In the Euler equation the $1/a^2$ term is the peculiar acceleration, the deviation of velocity from the Hubble flow due to inhomogeneities in density and is the term that facilitates gravitational collapse. Equations 1.12, 1.13, 1.14 can be combined while assuming $\delta = 0$ but $\dot{\mathbf{x}} \neq 0$ (a vortical field) to give

$$\ddot{\delta} + 2H\dot{\delta} - 4\pi G\rho_b\delta = 0. \tag{1.16}$$

This equation can be solved analytically for an Einstein-de Sitter (EdS) universe in which $\Omega = \Omega_m = 1$. An EdS model universe is one of only matter and can be used to approximate the matter dominated epoch of our own Universe which occurred at $\approx 0.33 < z < 10^4$. In an EdS the background density evolves with time as

$$\rho_b = \frac{1}{6\pi G t^2}, \tag{1.17}$$

and the Hubble parameter

$$H = \frac{2}{3t}. \tag{1.18}$$

Inserting these into equation 1.16 gives

$$\ddot{\delta} + \frac{4}{3t}\dot{\delta} - \frac{2}{3t^2}\delta = 0. \tag{1.19}$$

Trying a solution of the form $\delta \propto t^n$ finds a growing mode solution of $n = 2/3$ (and a decaying mode of $n = -1$ which can be ignored). This solution can be written as

$$\delta(\mathbf{x}, a) = D(a)\delta_0(\mathbf{x}), \tag{1.20}$$

with $\delta_0(\mathbf{x})$ the linear overdensity field today. This solution implies, for $\Omega_m = 1$, $D(a) \propto a$ or small perturbations grow at the same rate as the scale factor everywhere.

The Zel'dovich approximation, (Zel'dovich 1970), extrapolates linear theory outside of $\delta > 1$. It recasts the equations using the full convective derivative and evaluates them from an initial position at $a \approx 0$, $\mathbf{q}$, which leads to an equation for the Eulerian position

$$\mathbf{x}(a) = \mathbf{q} - \nabla_x \Phi(\mathbf{q}) D(a), \tag{1.21}$$

with $D(a)$ the linear growing mode solution. This can then be applied to an overdense region that is collapsing. Considering two particles that are near to each other within the collapsing region with initial separation $d\mathbf{q}$, then later $d\mathbf{x}$, a deformation tensor can be found. This tensor can be diagonalised by choice of coordinates and the density can be found by following the separation of the two particles to give

$$\frac{\rho(\mathbf{x})}{\rho_{b,0}} = \frac{1}{(1 - D\lambda_1)(1 - D\lambda_2)(1 - D\lambda_3)}, \tag{1.22}$$

where λ_i are the eigenvalues of the deformation tensor (the values along the diagonal for a diagonal matrix). A perfectly spherical perturbation would have $\lambda_1 = \lambda_2 = \lambda_3$ but in practice a triaxial perturbation, $\lambda_3 < \lambda_2 < \lambda_1$, is more realistic. This leads to collapse across three axes, initially collapsing across the shortest axis, λ_1, (the bigger the eigenvalue, the smaller the axis). This is known as shell crossing and a region of space that undergoes shell crossing is known as a caustic. Initially the caustic is a 2D ellipse called a sheet, then a 1D line, a

filament, then finally a point, a halo.

1.2.2 Halo Evolution

For a halo, assuming a spherical perturbation with constant density and in EdS, a spherical top hat model can be used to model the evolution of its radius. Starting from the Friedmann equation with R the physical radius

$$\dot{R}^2 = \frac{8\pi G}{3}\frac{\rho_{b,0}}{R} = \frac{\alpha^2}{R}, \tag{1.23}$$

where α is the cosmological scale factor. The background solution for a region of space at mean density can then be written as

$$R(t) = \left(\frac{3\alpha}{2}\right)^{2/3} t^{2/3}. \tag{1.24}$$

The radius of a spherical region with the same mass but overdense ($r < R$) evolves as

$$\dot{r}^2 = \frac{\alpha^2}{r} - \epsilon^2, \tag{1.25}$$

where ϵ^2 implies positive curvature. The solution to this equation is one of a cycloid

$$r(\theta) = A[1 - \cos(\theta)], \tag{1.26}$$

$$t(\theta) = B[\theta - \sin(\theta)], \tag{1.27}$$

with

$$A = \frac{\alpha^2}{2\epsilon^2}, \tag{1.28}$$

$$B = \frac{A}{\epsilon}. \tag{1.29}$$

The background radius can then be recast as

$$R(t) = A(9/2)^{1/3}(t/B)^{2/3}, \tag{1.30}$$

and the linear solution for the evolution of the radius of an overdense sphere can be shown to be

$$r_{lin}(t) = R(t)\left[1 - \frac{1}{20}\left(\frac{6t}{B}\right)^{2/3}\right]. \tag{1.31}$$

This model quickly breaks down as $\delta_{lin} > 1$ but still holds useful results, particularly at collapse where in reality $\delta = \infty$ but linear theory predicts $\delta_{lin} \approx 1.69$. If a halo is defined as being a region of virialised matter when collapsed then, using virial theorem, $2K + V = 0$ with K, V the total kinetic/potential energy of the halo and assuming conservation of energy for a viralised object the total energy is given by $E = V/2$. When linear theory predicts the radius to stop expanding and start shrinking (turnaround) $K = 0$, thus one can find $E = V_{ta}$ and $V/2 = V_{ta}$ from the energy equation. Recalling that the mass M of the region is constant by design the radius can be found as $r = r_{ta}/2 = A$. Finally assuming virialisation is complete by the time of collapse results in $t_{coll} = 2t_a = 2\pi B$. These can all be used to work out the relative density of a virialised halo

$$\Delta_c = \rho/\rho_b = \left(\frac{R}{r}\right)^3 = 18\pi^2 \approx 178. \tag{1.32}$$

Due to the approximations involved generally, $\Delta_c = 200$ is used as the density of a virialised halo over background. Noting that a halo is a sphere, the virialised

radius and mass (the radius containing the $\Delta_c = 200$ density and the total mass within that radius) can be defined as

$$M_{200} = \frac{4\pi}{3} R_{200}^3 200 \rho_{cr}. \tag{1.33}$$

1.2.3 Gas in the Universe

While haloes are formed from dark matter collapsing, it is the baryons in the Universe we directly observe. It is important to understand how baryons came to be in the IGM and within haloes and how they originated from just after the big bang.

In the seconds after the big bang it is theorised that the Universe was composed of both matter and antimatter and was dominated by radiation. The Universe that has been observed contains only matter and lacks voids big enough to allow antimatter regions to exist thus, there must have been a small amount more matter than antimatter, which was left over after the rest had annihilated with each other. This is supported by the observation that the photon to baryon ratio is so high, $n \approx 6 \times 10^{10}$, when initially they were in equilibrium (Komatsu et al. 2011). This epoch is known as Baryogenesis. Following this, as the temperature passed 1 MeV, the thermal energy of the Universe became comparable to nuclear binding energies. Initially neutrons and protons were in equilibrium

$$n + \nu_e \rightleftharpoons p + e^-, \tag{1.34}$$

$$n + e^+ \rightleftharpoons p + \bar{\nu}_e, \tag{1.35}$$

but, since p and n have different masses these processes can create/require energy, $m_n c^2 - m_p^2 = 1.29$ MeV. Neutrons also decay via $n \rightarrow p + e + \bar{\nu}_e$ with a half-life of 900s. When in equilibrium the number of protons and neutrons follows the

Maxwell Boltzmann distribution

$$n_n = 2\left(\frac{m_n k_B T}{2\pi\hbar^2}\right)^{3/2} exp\left(\frac{-m_n c^2}{k_B T}\right), \tag{1.36}$$

$$n_p = 2\left(\frac{m_p k_B T}{2\pi\hbar^2}\right)^{3/2} exp\left(\frac{-m_p c^2}{k_B T}\right). \tag{1.37}$$

Since $m_n \approx m_p$ the ratio can be simplified to

$$\frac{n_n}{n_p} = exp\left(\frac{-1.29\text{MeV}}{k_B T}\right), \tag{1.38}$$

which cannot be correct as it implies an exponential decline in the number of neutrons as the Universe cools, i.e after 5 minutes $n_n/n_p \approx 10^{-6}$. This is remedied when considering the reactions are via the weak force, which provides a high cross section for the interactions only at high temperatures. The total rate of reactions is given as $\Gamma \propto t^{-5/2} \propto a^{-5}$, i.e. reaction rate decreases drastically with time, thus eventually $\Gamma = 1/H_0$, or one interaction per Hubble time (age of the Universe). This is known as Freezeout and occurs at $T_{freeze} = 9 \times 10^9$K, with the neutron to proton ratio ≈ 0.2. At this point nucleosynthesis begins in which proton chains form Deuterium, which then further reacts to form Helium and fusion continues until all the neutrons are locked in Helium. Using the n_n/n_p ratio the mass fraction of He is found to be 1/3 but, when considering the decay of neutrons and that they can be locked in heavier elements, this number has been observed to be 0.24 (Komatsu et al. 2011).

In the early Universe, after nucleosynthesis, it is predicted by the ΛCDM model that it was too hot for neutral atoms to exist. Instead the Universe was an opaque plasma from which photons could not escape due to the Thomson scattering from the charged particles. At $z \approx 1100$, as the Universe expanded and cooled, recombination occurred in which neutral hydrogen could form, allow-

ing photons to escape via the de-excitation of the neutral hydrogen's electrons. This escape of the photons is known as last scattering and is what is observed as the CMB. Much later, as the dark matter began collapsing the baryons followed. This caused the baryons in gas to form the same caustic structures as the dark matter which led to the observed structure of the Universe, the cosmic web (figure 1.1) in which haloes are connected by filaments and sheets to other haloes. As gas collapses it gains kinetic energy until it produces shocks which subsequently heat it causing regions of hotter gas to form such as in halos. This hotter gas then cools via different radiative methods creating the necessary environments for star formation. Finally, at $z \approx 8$, the first stars and galaxies formed and UV photons radiated from them and escaped, photo-ionizing the IGM. This is known as reionization in which the gas in the Universe reverted to an ionized plasma but at a low density, which is how it remains to this day (Planck Collaboration et al. 2020b).

The gas can be split up into four different phases based on its temperature and density: warm gas; warm-hot gas; hot gas; and condensed gas which is important as these groups determine what emission/absorption lines are seen in observations (table 1.2). In collapsed objects there are further effects to consider. As before, gas gains thermal energy via shock accretion but, in haloes, the gas eventually settles into hydrostatic equilibrium in which the pressure gradient of the gas balances the inward force of gravity. The temperature of the gas in hydrostatic equilibrium is known as the virial temperature (T_{200}) and an expression can be derived from the singular isothermal sphere (SIS) model which assumes constant T and a 1D velocity dispersion σ. Starting from the Euler equation with velocity $\mathbf{v} = 0$

$$\nabla P = -\rho \nabla \phi, \tag{1.39}$$

Phase	Temperature(K)	log Hydrogen Density(cm^{-3})
Warm	$T < 10^5$	$n_H < -1$
Warm-hot	$10^5 < T < 10^7$	$n_H < -1$
Hot	$T > 10^7$	$n_H < -1$
Condensed	–	$n_H > -1$

Table 1.2: The identifiers for the different phases of gas seen in the Universe at $z = 0$. For this work, when using the density thresholds at different redshifts, the hydrogen density is scaled to compensate for the expansion of the Universe. Condensed gas is only defined by its density and the threshold was picked to encompass all star forming gas (Schaye et al. 2015).

with ρ, P, ϕ the gas density, pressure and total gravitational potential. When assuming spherical symmetry this can be written as

$$\frac{dP}{dr} = -\frac{GM(<r)}{r^2}\rho, \tag{1.40}$$

with M the total integrated mass. The assumption of an isothermal ideal gas

$$P = \rho kT/\bar{m}, \tag{1.41}$$

with $\bar{m}$ the mean mass of a gas particle can be used to show

$$\frac{dP}{dr} = \frac{kT}{\bar{m}}\frac{d\rho}{dr}. \tag{1.42}$$

It then follows that

$$\frac{kT}{\bar{m}}\frac{dln(\rho)}{dln(r)} = -\frac{GM}{r}, \tag{1.43}$$

which can be rearranged while setting $r = R_{200}$ to get the virial temperature

$$T_{200} = \frac{G\bar{m}}{2k}\frac{M_{200}}{R_{200}}. \tag{1.44}$$

In haloes radiative cooling occurs that causes cool gas to end up in the halo's centre. At lower temperatures, $10^4 < T(\mathrm{K}) < 10^7$, excitation cooling dominates

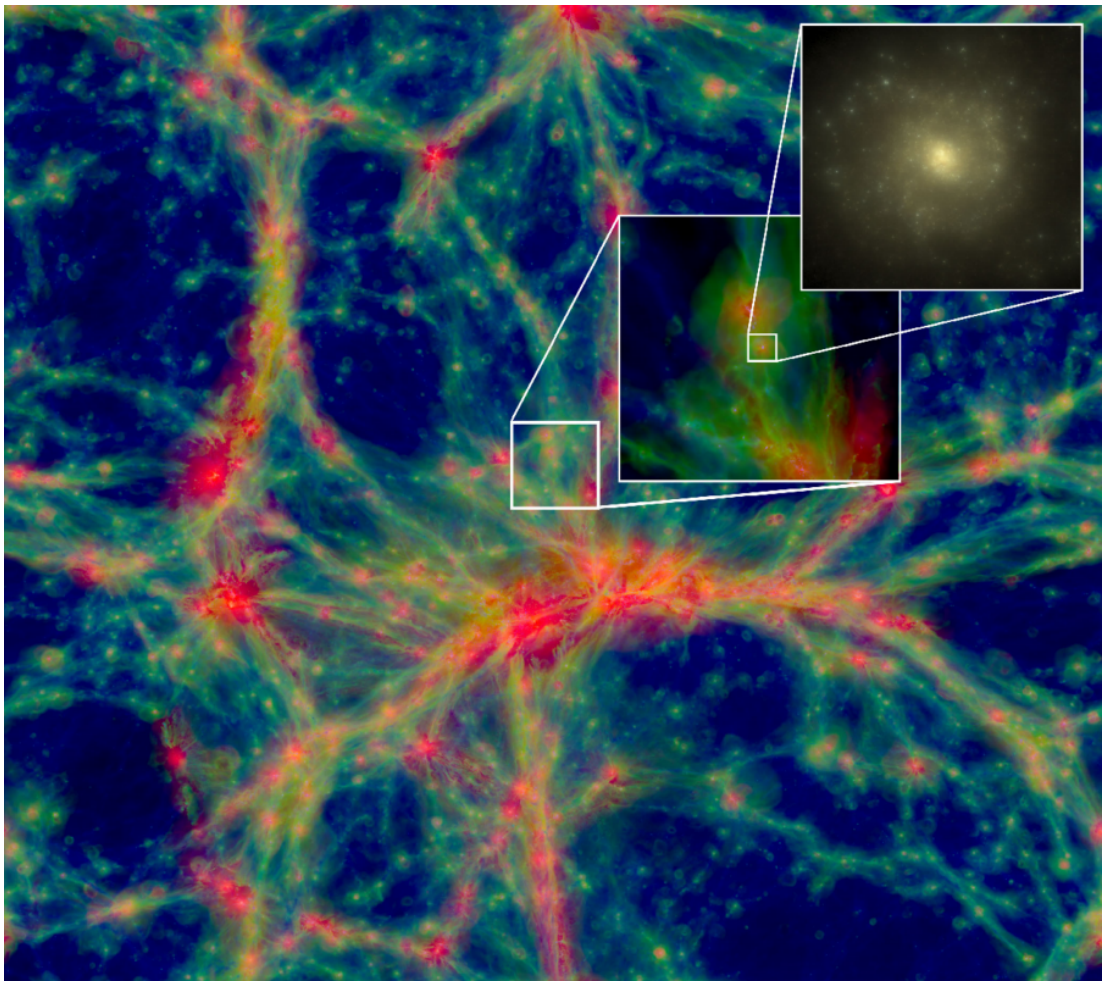

Figure 1.1: An example of the cosmic web from the EAGLE simulation in a $100\times100\times20$ comoving Mpc slice with blue, green, red indicating $T < 10^{4.5}$K, $10^{4.5}$K $< T < 10^{5.5}$K, $T > 10^{5.5}$K and the intensity tracing density. Taken from Schaye et al. (2015).

which involves electrons being excited then reverting to the ground state, releasing a photon which takes energy away from the particle, thus cooling it. At higher temperatures, $T > 10^7$K, free-free bremsstrahlung dominates in which free electrons are decelerated when passing an ionised nucleus and then the excess energy is radiated away as a photon. For smaller galaxies, $M_{200} < 10^{12} M_\odot$, cooling is efficient and all gas within the halo quickly cools. They then fall to the centre due to lack of pressure for hydrostatic equilibrium and form a central galaxy. For larger galaxies/collapsed objects, $M_{200} > 10^{12} M_\odot$, cooling is less efficient (when

ignoring metal line cooling) leading to slower cooling of the gas within the object and more of it remaining at $\approx T_{200}$.

Once a galaxy has formed different feedback mechanisms begin to affect their evolution. One such is Supernova feedback, in which massive stars ($M > 8M_{\odot}$) collapse (core collapse Type II SNe) and release energy on the order of $E_{sn} = 10^{44}$J. Supernovae release enough energy for gas to escape galaxies but not enough to escape groups or clusters in which supernova feedback becomes less important.

More important for groups and clusters are black holes at the galaxy centre which can be active galactic nuclei (AGN) that produces feedback. An idealised model for how AGNs accrue mass is the Bondi-Hoyle-Lyttleton formula

$$\dot{M}_{BH} = \frac{4\pi G^2 M_{BH}^2 \rho_{gas}}{(c_s^2 + v^2)^{3/2}}, \tag{1.45}$$

with ρ_{gas}, c_s and v the gas density, speed of sound and flow speed respectively. A black hole will eventually reach the Eddington limit in which the outwards radiation pressure balances the inward force of gravity

$$\dot{M}_{Edd} = \frac{4\pi G m_H c}{\epsilon_r \sigma_T c} M_{BH}, \tag{1.46}$$

with ϵ_r the accreted mass to energy efficiency factor ($\epsilon_r \approx 0.1$) and σ_T Thomson cross section. AGNs radiate gas via relativistic jets and non-relativistic X-ray outflows. This leads to balancing the black hole's growth and the removal of gas from the collapsed object (Krolik and Di Matteo 2000).

1.3 The Missing Baryon Problem

As explained in subsection 1.2.3 there is a fixed amount of baryons in the Universe. Studies of the CMB and Big Bang nucleosynthesis (Planck Collaboration

et al. 2020b; Komatsu et al. 2011) have obtained a value for this baryon density fraction (table 1.1), but in the low redshift Universe ($z < 1$), a deficit has arisen. At $z = 0.4$, $\approx 29\%$ of baryons are unaccounted for, with $18\% \pm 4\%$ of baryons in collapsed haloes (galaxies, groups, clusters and the circumgalactic medium (CGM)), $28\% \pm 11\%$ in the Ly-α forest, $(28\% \pm 8\%)$ in the OVI traced warm-hot intergalactic medium (WHIM) and $25\% \pm 8\%$ in broad-Ly-α absorbers (Shull et al. 2012). The Ly-α forest is observations of absorption lines from the spectra of distant galaxies/ quasars when passing through neutral hydrogen. This results in the Lyman-alpha transition, the transition of an electron from the $n = 1$ to the $n = 2$ energy level of neutral hydrogen, allowing for the detection of these baryons.

The missing baryons have been theorised to exist in the WHIM and should be detectable via 0.25 keV X-ray emission (Davé et al. 2001). These X-rays will be very faint due to the emission source gas being very diffuse and as a result there have been very few direct observations (Tanimura et al. 2020; Nandra et al. 2013).

Another method that has been used to locate the WHIM is the thermal Sunyaev-Zel'dovich effect. This involves photons from the CMB passing through ionised gas, such as the WHIM, and undergoing inverse Compton scattering. This is a free-free interaction in which incident photons deflect off free electrons gaining energy. When this effect occurs in the WHIM the fractional energy change of the CMB photons depends only on the electrons along the line of sight and temperature thus making them good probes for the missing baryons. Similar to the x-ray emission, an issue with this method is, it must contend with a weak signal due to the diffuse nature of the gas under inspection (Birkinshaw 1999; Tanimura et al. 2019).

The missing baryon problem was raised in a number of papers (Cen and Ostriker 1999; Davé et al. 2001; Fukugita 2004). In Cen and Ostriker (1999) a cold

dark matter simulation was used to predict that the missing baryons would be observable within the soft x-ray band, the wavelength due to the same temperature range as the Warm-Hot gas phase. In Davé et al. (2001) another set of hydrodynamical simulations was used to find the gas fraction within the WHIM, with the result they found $\approx 30 - 40\%$. A more recent examination of the problem was carried out in Shull et al. (2012) which compared observational data, OVI absorption lines from the Hubble Space Telescope and IGM data from the Far-Ultraviolet Spectroscopic Explorer, to an improved N-body simulation, Enzo. They found that $29\% \pm 13\%$ of baryons were still unaccounted for but suggested that $\approx 15\%$ exists in the hot WHIM ($T > 10^6$K). In Nicastro et al. (2018) by observing an x-ray spectrum of a quasar through intervening highly ionized oxygen (OVII) it is claimed they have directly measured the WHIM, that their results agree with simulation predictions and the "missing baryons in the WHIM have been found".

1.4 Fast Radio Bursts

While other methods of detecting the WHIM have been summarised, the method used in this thesis is measuring the dispersion measure from fast radio bursts (FRBs).

FRBs are extra-galactic transients, characterised by brief radio pulses that exhibit a large dispersion in time detected across the different frequency components that make up the burst. They are bright ($50\text{mJy} - 100\text{Jy}$); with frequencies between $400\text{MHz} - 800\text{GHz}$; only last for milliseconds or less; and small numbers have been observed creating repeat signals (Petroff et al. 2019). The origins of FRBs are currently unknown with the location of origin only recently being constrained to galaxies (Chatterjee et al. 2017; Macquart et al. 2020). Recent work has indicated that they may be from a subset of magnetars, stars formed from

a rapidly rotating neutron star at birth possibly via neutron star mergers. This causes the neutron star to be highly magnetised, producing bigger flares that are in line with both the energy detected from the burst and the ability to repeat (Metzger et al. 2017).

FRBs offer an opportunity to study the structure of the Universe as the time delay between the frequencies is dependent on the amount of electrons the burst passes through. This leads to a dispersion measure (DM), a measure of the electron density passed, weighted by $(1+z)^{-1}$ to account for the expansion of the Universe. This can be found by integrating over the total distance travelled by the FRB

$$DM_{FRB} = \int_0^l \frac{n_e(z)}{1+z} dl, \tag{1.47}$$

with n_e the physical electron density and dl the physical distance element given by

$$dl = c(1+z)^{-1} H_0^{-1} E(z)^{-1} dz, \tag{1.48}$$

where

$$E(z) = \sqrt{\Omega_m (1+z)^3 + \Omega_\Lambda}, \tag{1.49}$$

for a flat late universe model ($\Omega_k = \Omega_r = 0$), with c the speed of light, H_0, the Hubble constant.

FRBs originate from distant galaxies thus the DM can be broken up into its different components

$$DM_{FRB}(z) = DM_{MW} + DM_{cosmic}(z) + \frac{DM_{Host}}{1+z}, \tag{1.50}$$

with DM_{MW}, DM_{cosmic}, DM_{Host} the contribution of electrons in the Milky Way, the IGM and the FRB host galaxy respectively. DM_{MW} is well constrained by galaxy electron density models (Cordes and Lazio 2002; Yao et al. 2017) and at high latitudes ($> 33\,\mathrm{deg}$) has been measured by Australian Square Kilometre Array Pathfinder (ASKAP) as $\approx 30\mathrm{pc\ cm^{-3}}$ not including the Milky ways CGM (Macquart et al. 2020), which is less well constrained. DM_{Host} is far less well constrained due to the uncertain origin of FRBs and could vary wildly depending on the local conditions. DM_{cosmic} is the most useful tool for inferring information on the structure of the Universe and acts as a way to detect the missing baryons.

DM_{cosmic} can be calculated for a homogeneous universe at mean density and should be the mean value for all FRBs at the same distance when ignoring host or Milky Way contributions. Starting from eq.1.47 the electron density for a homogeneous universe can be written as

$$n_e = \frac{\rho_b}{\mu_e m_p} = \frac{\Omega_b \rho_{c,0}}{\mu_e m_p}(1+z)^3, \tag{1.51}$$

where μ_e is the mean molecular weight per free electron (≈ 1.1 for fully ionised primordial plasma) and m_p is the mass of a proton and the critical density

$$\rho_{c,0} = \frac{3H_0^2}{8\pi G}. \tag{1.52}$$

This leaves

$$DM = \frac{\Omega_b \rho_{c,0}}{\mu_e m_p} \int_0^z (1+z)^3 \frac{dl}{dz} dz. \tag{1.53}$$

Converting dl to dz can then be done by considering $dl = -cdt$ then noting $\dot{a}/a = H(t)$ and $a = 1/(1+z)$ giving eq.1.48. Putting it all together, and using the definition for $\rho_{c,0}$ gives

$$DM_{cosmic} = \frac{3cH_0\Omega_b}{8\pi G\mu_e m_p}\int_0^z \frac{(1+z)}{\sqrt{\Omega_m(1+z)^3+\Omega_\Lambda}}dz. \tag{1.54}$$

This equation assumes all gas in the Universe is ionised and homogeneously distributed and is generally solved numerically. As in Shull et al. (2012), the DM-z relation can be used to find the missing baryons using the fact that the DM counts all the electrons along its path, including those from the missing baryons.

1.5 Past Works on FRBs as a probe

There have been recent studies using the DM of FRBs to locate the missing baryons (McQuinn 2014; Macquart et al. 2020; Zhang et al. 2021; Batten et al. 2021). McQuinn (2014) studies how well suited FRBs are for locating the missing baryons. They considered the statistics and particularly the scatter of the DM along with the contamination from the host galaxy but, concluded that the method could constrain the location of the cosmic baryons. Macquart et al. (2020) used observed FRBs with known host galaxies/ redshifts and compared them to eq.1.54 while also considering the contributions from the Milky Way and the host galaxies. They found their gold standard sample of FRBs (five FRBs) to all fall within 90% of a model involving ejective feedback from galaxy haloes, and concluded their FRB ensemble to have "resolved the missing baryon problem".

A number of recent papers have applied the method of DMs from FRBs to modern N-body, hydrodynamical simulations. This has been done to test the simulations compared to observations, give predictions for DMs and analyse the statistics of a larger sample size than possible with just the current observed FRBs (Zhang et al. 2021; Batten et al. 2021). Zhang et al. (2021) used the IllustrisTNG simulation for its analysis and created synthetic sight lines that were stacked across snapshots to mimic the path taken by a FRB though the Universe.

The electrons within these sight lines were then directly counted to get the DM which was compared to eq.1.54 and the distribution of the residuals was found to be a "quasi-Gaussian function with a long tail". Zhang et al. (2021) also probed higher redshifts ($z < 6$) and concluded that "high-redshift FRBs are promising probes of the cosmic reionization history".

Batten et al. (2021) applied similar analysis using the EAGLE simulation. They considered the ionization state of the gas using a spectral synthesis program called Cloudy which affects the number of electrons. This is since EAGLE does not contain the details of electrons, only the gas. They then stacked the 100 Mpc EAGLE boxes at different redshifts to build a sight line and compared their data up to $z = 3$, with the average over $\approx$ one billion sight lines, against the background, eq.1.54 but with an additional factor that depends on z to account for a partially ionised IGM. To avoid repeating structure when stacking the same box they randomly reassigned the line through each box to new locations. They found a linear fit for the DM redshift relation, $DM_{cosmic} = 999.4z + 17.0$, and a skewed Gaussian fit for the residuals.

This thesis will present the findings of the EAGLE simulation, simulating FRBs from cosmological distances. An overview of the simulation and a description of the techniques employed to simulate FRBs is given in Chapter 2 including: n-body solvers; hydrodynamics; EAGLE's initial conditions; the subgrid physics; and how haloes are identified. In Chapter 3 the results of the analysis conducted are presented. In section 3.1 the analysis done by Batten et al. (2021) is followed using a smaller box size (50 Mpc/h) and the results are compared including a comparison to observed FRBs with known host galaxies. In section 3.2 the investigation is extended to test how the hot gas in haloes contributed to the signal along with how the mass of the host halo affects the DM. In section 3.3 how the DM depends on gas of different density intervals is explored. Finally, in Chap-

ter 4, a summary of the results; the conclusions; and potential opportunities for future work are presented.

Chapter 2

Method

2.1 Simulations

Modern simulations provide a model universe built upon dark matter that acts as a sandbox, enabling cosmology and galaxy formation theories to be tested in a near endless set of different environments that observations cannot offer. Observations also cannot directly measure dark matter which is key to structure formation. Simulations are used to interpret these observations and guide the direction of new instruments (Euclid Collaboration et al. 2021).

This chapter will look at the methods used to calculate the dynamics of particles in the simulation, starting with dark matter and then baryonic matter. The details of the EAGLE simulation are then summarised in section 2.2 including the initial conditions, hydrodynamics, subgrid physics and the Friends-of-Friends (FoF) algorithm. Finally, the method implemented for simulating the DM from FRBs is described in section 2.3

2.1.1 Gravity Calculation

Both the baryons and dark matter move according to gravity but baryons in gas have other properties that affect their dynamics. The evolution of collisionless dark matter only depends on gravity and, to simulate them, N-body methods are used.

These methods follow the non-linear behaviour of collapse and involve a distribution of N particles in a cube that exists within a position/velocity phase space. The cube has periodic boundaries following the cosmological principle. A power spectrum, a function that encompasses all the information about the initial field, is then used to determine each particle's location within the phase space. The particles are then perturbed from their initial uniform distribution. When used in cosmological simulations the particles act as mass tracers, and the total mass within the cube will have, by design, the mean density of the Universe. To then simulate how mass evolves over time the peculiar acceleration must be calculated from the gravitational force. There are a number of ways this is done including: direct summation; Oct-tree; and Particle-mesh.

Direct summation is the simplest method and involves summing the gravitational force contribution from each particle, for each particle (equation 2.1). This is an exact method but is very slow to run as the computational time scales with number of points squared, $O(N^2)$. The sum for the gravitational potential gradient felt by a particle is given as

$$\nabla_{\mathbf{x}}\phi = Gm^2 \sum_{j=1,j\neq i}^{N} \frac{\mathbf{x}_i - \mathbf{x}_j}{|\mathbf{x}_i - \mathbf{x}_j|^3}, \tag{2.1}$$

with $\nabla_{\mathbf{x}}$ the comoving gradient operator, ϕ the gravitational potential, G, the gravitational constant, m, the particle's mass, $\mathbf{x}_i$ the particle's position, $\mathbf{x}_j$ the position of the particles applying the force and N, the number of particles in the

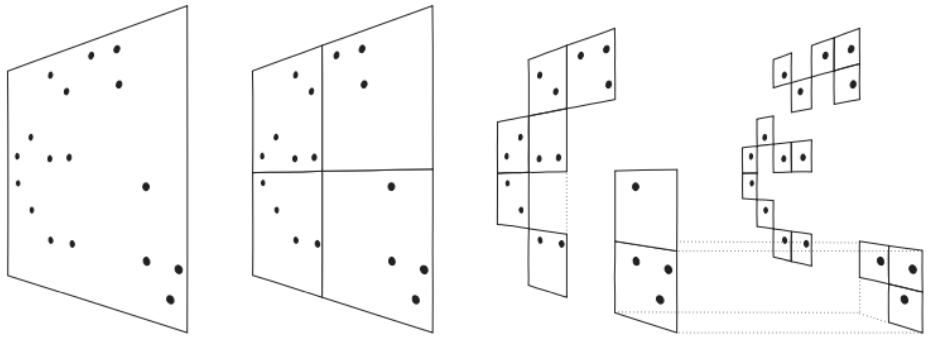

Figure 2.1: A diagram showing how a tree structure is constructed by segmenting different areas of the cube. Taken from Springel et al. (2001b).

simulation.

A way to speed this up is the Oct-tree method in which the cube is divided into eight cells (octant) which are then themselves subdivided into daughter cells (branches). This subdivision continues until a branch has only one particle (leaf) (figure 2.1). Each branch then points to parent, child and sibling branches which are stored along with the total mass and centre of mass of particles within each branch. The force on any particle is then calculated by performing a tree walk (method illustrated in figure 2.1). Starting from the top branches the force calculations only includes the cells that pass the condition $l/D < \theta$, where l is the length of the branch currently being processed, D is the distance from the particle to the branch's centre of mass and θ is some accuracy parameter that is ≈ 1 (Barnes and Hut 1986). Once the condition is fulfilled for a branch the calculation stops and uses the upper branches for the acceleration. This method is fast (computational time scales with $O(Nln(N))$) and accurate for a non-uniform distribution of particles but less accurate for more uniform distributions (e.g. the largest cosmological scales or at early times in the Universe) and assumes that small scale structure is not important.

The final method is the Particle-mesh method. It solves the Poisson equation on a cubic mesh of N_{cells} per side. It then calculates the overdensity for each mesh point and uses the fast fourier transform (FFT) to find the fourier modes. The inverse FFT is then used to calculate the potential on the mesh. Finally it finds the gradient across nearby meshes and interpolates the accelerations onto the particles. This method is fast ($O(Nln(N))$) and good for a uniform distribution. It is however, very memory intensive, scaling as N^3, and is resolution limited by the mesh spacing.

The Gadget-3 code, which underlies the code used in this thesis, uses a hybrid of the Particle-mesh and Oct-tree methods. This has been done by using the Particle-mesh method to solve for long range forces and the Oct-tree method solve for short range forces then summing for the total force on a particle. This has the advantages of both methods while mitigating the disadvantages (a full description of how this is implemented can be found in section 3.2 of Springel (2005).

2.1.2 Baryons

For baryons different methods are used for the calculation of dynamics due to additional properties to consider. Semi-analytic models are used to track the evolution of gas only in dark matter haloes including: gas cooling; galaxy formation; and star formation. It can also be used to include the growth of black holes and active galactic nuclei (AGN) feedback (Bower et al. 2006). An alternative is hydrodynamic simulations. These simulate both dark and baryonic matter over the whole box in which the gas is assumed as an inviscid ideal gas and follows the Euler equations but including a non-zero pressure term

$$\frac{\partial \mathbf{v}}{\partial t} + \mathbf{v} \cdot \nabla \mathbf{v} + \frac{\nabla P}{\rho} + \nabla \phi = 0. \tag{2.2}$$

One such method is smoothed particle hydrodynamics (SPH) (Gingold and Monaghan 1977). It is a Lagrangian method that smooths the baryon particles (blobs with set parameters, not physical particles) with a kernel, W and width, h.

$$\langle A(\mathbf{r})\rangle = \int A(\mathbf{r}')W(|\mathbf{r}-\mathbf{r}'|,h)d^3r', \tag{2.3}$$

where h is the comoving smoothing length scale. This has the advantages that it is fast, memory efficient and is suited to a large dynamic range for calculations such as in galaxy formation. Its disadvantages include no defined boundary and worse performance/accuracy with discontinuities such as fluid instabilities, which must be fixed with artificial viscosity and diffusion terms. Hydrodynamics must also be augmented with astrophysical processes that affect galaxy formation as the numerical resolution of current simulations is limited.

2.2 EAGLE

The simulation used in this thesis is the Evolution and Assembly of GaLaxies and their Environments (EAGLE) project (Schaye et al. 2015). EAGLE is a modified version of the GADGET-3 code which uses a N-Body hybrid Tree-PM method, Tree for short range and PM for long range gravitational forces. It has three box sizes, 25cMpc/h, 50cMpc/h, 100cMpc/h with cMpc a comoving megaparsec, a unit of distance that stays constant over time by factoring out expansion and h the dimensionless Hubble constant. For the baryons a smoothed particle hydrodynamics (SPH) method is employed (Springel 2005).

2.2.1 Initial Conditions

The full details of the production of initial conditions can be found in the appendix of Schaye et al. (2015) but are summarised below.

Firstly, particles representing a homogeneous periodic universe in a 3 dimensional torus are produced using a "glass-like" particle distribution of 47^3 particles (White 1994). Then the particles are perturbed using a Gaussian random field that is created from the Panphasia software resulting in Zeldovich initial conditions (Jenkins 2013). EAGLE is then used to solve a Poisson equation for this mass, resulting in the second order Lagrangian growing mode displacements and velocities for each particle. These growing modes are consistent with the real growing modes due to gravitational instability. Using these on the particle displacements and velocities produces the final second order Lagrangian perturbation theory initial conditions. The evolution with time for the dark matter particles can then be calculated using the equations of motion.

For baryons the initial conditions are created by replacing each dark matter particle with a pair, one dark matter and one baryon particle which have a combined mass equal to the original dark matter particle being replaced. The ratio of dark matter to baryonic matter particles is then $\Omega_b/(\Omega_m - \Omega_b)$ (the constants used in EAGLE can be found in table 2.1). The pair of particles are arranged such that their centre of mass is the same as the original. Using these particles an initial cubic grid at mean density with the dark matter only initial conditions would transform into a body-centred cubic grid with a dark matter/ baryon particle at its centre surrounded by gas/ dark matter on the other axes.

2.2.2 Hydrodynamics

EAGLE modifies the GADGET-3 SPH to remedy issues with its use. In particular the large artificial viscosity, which is required to capture shocks, causes unphysical surface tension at discontinuities such as the Kelvin-Helmholtz instabilities which occur when a velocity shear between two fluids is present (Agertz

Parameter	Value
Ω_m	0.307
Ω_Λ	0.693
Ω_b	0.04825
h	0.6777
σ_8	0.8288
Y	0.248

Table 2.1: The values used in the EAGLE simulation with h the dimensionless Hubble constant, σ_8 the root of the linear variance of matter distribution when smoothed using a top hat filter of radius $8h^{-1}$cMpc and Y the primordial helium abundance (Schaye et al. 2015)

et al. 2007). EAGLE uses "ANARCHY", a set of alterations to the vanilla SPH that improves upon the base GADGET-3 implementation (Schaller et al. 2015).

ANARCHY SPH uses a different smoothing kernel function than GADGET-3

$$W(r,h) = \begin{cases} (\frac{21}{2\pi h^3})(1-\frac{r}{h})^4(1+4\frac{r}{h}), & \text{if } 0 \leq r \leq h, \\ 0, & \text{if } r > h, \end{cases}$$

where h is the smoothing length and r is the distance from the particle. The dynamics of the particles are based on the equations from the pressure-entropy formulation from Hopkins (2013) which itself is a generalisation of earlier works (Ritchie and Thomas 2001; Read et al. 2010). Density, entropy and velocity for the particles are integrated over time along with additional, smoothed quantities including the weighted density

$$\bar{\rho}_i = \frac{1}{A_i^{1/\gamma}} \sum_j m_j A_j^{1/\gamma} W(|\mathbf{x}_i - \mathbf{x}_j|, h_i), \tag{2.4}$$

and its associated weighted pressure $\bar{P}_i = A_i \bar{\rho}_i^\gamma$, with A_i the entropic function; $A_i = P_i/\rho_i^\gamma$, and γ the polytropic index. These smooth out the pressure jumps at discontinuities that a standard implementation of SPH would ignore. The velocities of the particles can then be found

$$\frac{d\mathbf{v}_i}{dt} = -\sum_j m_j \left[\frac{A_j^{1/\gamma}}{A_i^{1/\gamma}} \frac{\bar{P}_i}{\bar{\rho}_j^2} \Omega_{ij} \nabla_i W_{ij}(h_i) + \frac{A_i^{1/\gamma}}{A_j^{1/\gamma}} \frac{\bar{P}_j}{\bar{\rho}_j^2} \Omega_{ji} \nabla_j W_{ij}(h_j) \right], \tag{2.5}$$

with the smoothing length gradient term

$$\Omega_{ji} = 1 - \frac{1}{A_i^{1/\gamma}} \left(\frac{h_i}{3\rho_i} \frac{\partial \bar{P}_i^{1/\gamma}}{\partial h_i} \right) \left(1 + \frac{h_i}{3\rho_i} \right)^{-1}. \tag{2.6}$$

The artificial viscosity is added following Cullen and Dehnen (2010) in which each particle is assigned a viscosity α_i. The viscosity is calculated with

$$\dot{\alpha}_i = 2l\nu_{sig,i} \frac{\alpha_{loc,i} - \alpha_i}{h_i}, \tag{2.7}$$

where $l = 0.01$ and $\nu_{sig,i}$ is the signal velocity. The signal velocity is constructed in such a way that it captures the maximum velocity when information can be transferred between particles while positive, and $\alpha_{loc,i}$, the local viscosity estimator is given by

$$\alpha_{loc,i} = 2 \frac{h_i^2 S_i}{\nu_{sig,i}^2 + h_i^2 S_i}, \tag{2.8}$$

in which the shock detector is defined such that passing through a shock gives $S_i = 0$ and generally, $S_i = \max(0, -d/dt(\nabla \cdot \mathbf{v}_i))$. The final improvement for ANARCHY is the inclusion of entropy diffusion between particles. SPH is generally constructed in a way that does not include thermal conduction which may have an effect on the mixing of gas phases. ANARCHY includes a small amount of numerical diffusion that follows Price (2008). The internal energies from entropy are computed and then used in diffusion equations. The particles can now mix entropies which allow them to create a single phase and reduce the spurious pressure waves found in base SPH.

2.2.3 Subgrid Physics

While N-body and hydrodynamics solve for gravity and fluid properties, additional effects must also be included for a more complete description of the gas in the Universe. Subgrid physics implemented in EAGLE adds radiative cooling, reionization, star formation, stellar mass-loss/ metal enrichment, feedback from star formation and AGN feedback. A full description can be found in Schaye et al. (2015).

Radiative cooling

Following Wiersma et al. (2009a) who used CLOUDY (version 07.02), 11 elements that were found important in radiative cooling (H, He, C, N, O, Ne, Mg, Si, S, Ca, Fe) were modelled in the simulation, accounting for abundance and metallicity. Assuming ionization equilibrium and taking into account the effects of the CMB the cooling rates were calculated as a function of density, temperature and redshift.

Reionization

Reionization cannot naturally occur in the simulation so an artificial switch must be turned on. This was done using a time-dependent, spatially-uniform ionising background from Haardt and Madau (2001) at redshift $z = 11.5$ (consistent with Planck Collaboration et al. (2014)). To heat the gas an extra 2 eV per proton mass has been added that causes hydrogen to instantly reach $\approx 10^4$K in line with observations (Schaye et al. 2000). For HeII the heating is distributed over a redshift range following a Gaussian distribution centred at $z = 3.5$ with $\sigma(z) = 0.5$.

Star Formation

EAGLE lacks the resolution to directly model the cold ($T \ll 10^4$K) interstellar medium thus is also unable to directly model star formation. Stars have instead been inserted with formation rates that depend on pressure (Schaye and Dalla Vecchia 2008). This allows the Kennicutt-Schmidt star formation law (Kennicutt 1998) to be written as a pressure law

$$\dot{m}_\star = m_g A (1\mathrm{M}_\odot \mathrm{pc}^{-2})^{-n} \left(\frac{\gamma}{G} f_g P\right)^{(n-1)/2}, \tag{2.9}$$

where $\dot{m}_\star$ is the star formation rate, $\gamma = 5/3$ is the specific heat ratio, m_g is the gas particle mass, f_g is the mass fraction in the gas (assumed to be unity) and P is total pressure with A and n free parameters determined by observation. For the simulation these are $A = 1.515 \times 10^{-4}\mathrm{M}_\odot \mathrm{yr}^{-1}\mathrm{kpc}^{-2}$ and $n = 1.4$ which is increased to $n = 2$ for gas with $n_H > 10^3\mathrm{cm}^{-3}$ as there is some evidence to support this steepening (Genzel et al. 2010; Liu et al. 2011). This equation is implemented stochastically which causes gas particles to change into a collisionless stellar particle representing a population of stars. Star formation is limited to occur only in regions with gas above a density threshold that is dependent on metallicity

$$n_H^\star = 10^{-1}\mathrm{cm}^{-3} \left(\frac{Z}{0.002}\right)^{-0.64}, \tag{2.10}$$

in which Z is the fraction of the gas mass in elements heavier than helium (gas metallicity). To further limit star formation a minimum temperature of $T = 8000$K for densities of $n_H > 10^{-1}\mathrm{cm}^{-3}$ is imposed. This temperature is typical for the warm ISM. Once the temperature floor is no longer important, star formation follows the equation of state, $P \propto \rho_h^{4/3}$, normalized to $T = 8000$K at $n_H = 10^{-1}\mathrm{cm}^{-3}$ whose 4/3 slope prevents spurious fragmentation. To avoid stars forming in low density gas at high redshift, the gas density is required to be

a minimum of 57.7 times the cosmic mean.

Stellar feedback

The star particles are each stellar populations with an initial mass function (IMF) of $0.1 - 100\mathrm{M}_{\odot}$. The mass lost due to the stars is as prescribed in Wiersma et al. (2009b) and involves stellar winds along with core collapse Type II supernovae. At each time step, for each star particle, the number that reaches the end of the main-sequence phase is calculated (via metallicity). The fraction of the population reaching this phase along with the initial element abundances is used to calculate the mass lost due to stellar winds from the asymptotic giant branch (AGB) of stars for each element. The mass/ energy lost through Type 1a supernovae is also computed and the total mass lost is distributed to nearby SPH particles. This is done by using the SPH kernel, only using the 48 nearest neighbour particles. The fraction received by each particle is

$$\frac{m_p}{m_{tot}} = \frac{m_g}{\rho_k} W(r_K, h) / \sum_i \frac{m_g}{\rho_i} W(r_i, h), \tag{2.11}$$

where k indicates the neighbour particle, r_k is the separation from a star particle, h is the smoothing length, m_g the gas particles mass and ρ the density. The transfer of energy and momentum is also accounted for. The winds from the AGB stars are assumed to have a velocity of $10\mathrm{kms}^{-1}$ according to Bergeat and Chevallier (2005). The receiving gas particles have their velocities adjusted to conserve momentum and energy conservation is preserved by slightly changing their entropies.

For SNIa the rate of them occurring per unit mass is given as

$$\dot{N}_{SNIa} = \nu \frac{e^{-t/\tau}}{\tau}, \tag{2.12}$$

with ν the total number of SNIa per unit stellar mass and $\exp(-t/\tau)$ the nor-

malized, empirical delay time distribution function. This is applied every time step and the mass loss along with the energy and momentum is distributed to the neighbours. Energy is given as a stochastic thermal feedback model from Dalla Vecchia and Schaye (2012) which uses $\Delta T = 10^{7.5}\mathrm{K}$ and $10^{51}\mathrm{erg}$. Heating is done at the end of the type II phase (an age of $3 \times 10^{7}\mathrm{yr}$), once for each star particle. It is assumed in the simulation that the cooling is dominated by free-free emission and the value for ΔT comes from the expectation value for the number of heated gas particles per star particle

$$\langle N_{Heat} \rangle \approx 1.3 f_{th}(n, Z) \left(\frac{\Delta T}{10^{7.5}\mathrm{K}} \right)^{-1}, \tag{2.13}$$

where $f_{th}(n, Z)$ is the fraction of the energy from core collapse supernovae per unit stellar mass that is injected on average. The expectation value is given as $f_{th} = 1$ but $f_{th}(n, Z)$ depends on a number of different factors including metallicity and density. This, along with the model used, Chabrier IMF, only accounts for supernovae from stars in the range of $6 - 100\mathrm{M}_{\odot}$. Thus using $T \gg 10^{7.5}\mathrm{K}$ or $f_{th} \ll 1$ would cause most star particles to not inject any energy from their core collapse supernova into the surrounding particles.

Black holes and AGN feedback

AGN feedback from supermassive black holes must be included to produce realistic groups and clusters as they dominate the cooling in these larger haloes. Whilst supermassive black holes have poorly understood origins and their evolution with their host galaxy is still the subject of study, most of the processes occur on scales below what can be resolved by EAGLE (Kocsis and Loeb 2014).

Due to the resolution the direct formation of black holes cannot be modelled, instead, following Springel et al. (2005) black hole seeds are placed within the centre of all haloes that have a mass exceeding $10^{10}\mathrm{M}_{\odot}h^{-1}$ (the identification

of haloes is covered in the next subsection). The highest density gas particle within the halo is then converted into a collisionless black hole with a mass $m_{BH} = 10^5 \mathrm{M}_{\odot} h^{-1}$. This is stored in the subgrid as the mass of the particle is much larger than the mass of the black hole seed and must be preserved. The properties of the black hole, e.g. accretion rate, are calculated with the black hole seed's mass m_{BH}, whereas the gravitational force is found using the black hole particle's mass. Once m_{BH} exceeds the host particle's mass, it begins to stochastically accrete neighbouring SPH particles, causing the black hole particle's mass to grow in steps. To account for dynamical friction, black hole particles of mass less than 100 times their gas particles mass, $< 100 m_g$, are forced to move towards the point of minimum gravitational potential within the halo. This is done by moving the particle to the location of a neighbouring particle with the lowest gravitational potential that has a velocity relative to the black hole of $< 0.25 c_s$, with c_s the speed of sound, at each time step. This prevents black holes from jumping out of the seeded galaxy into nearby satellites.

The accretion rate is modelled depending on the local density, temperature, angular momentum and velocity relative to the ambient gas. The Bondi-Hoyle formula is then used (equation 1.45) and applying

$$\dot{m}_{accr} = \dot{m}_{Bondi} \times min(C_{visc}^{-1}(c_s/V_{\phi})^3, 1), \tag{2.14}$$

where the rotation speed V_{ϕ} is found using equation 16 of Rosas-Guevara et al. (2015) and C_{visc} is a free parameter set to 2π. The mass growth rate can be found as

$$\dot{m}_{BH} = (1 - \epsilon_r)\dot{m}_{accr}, \tag{2.15}$$

with ϵ_r the radiative efficiency of accretion. Black holes are merged when: their separation is less than the smoothing kernel of the more massive black hole (h_{BH});

three gravitational softening lengths; and their relative velocity is less than the circular velocity at the distance $h_{BH}, \nu_{rel} < \sqrt{G m_{BH} h_{BH}^{-1}}$. The velocity limit stops black hole pairs from merging in the initial stages of the galaxy merger.

AGN feedback is then implemented stochastically and thermally. The rate of energy injected is $\epsilon_f \epsilon_r \dot{m}_{accr} c^2$ with $\epsilon_f = 0.15$ the fraction of radiated energy coupled to the ISM, chosen based off observations and $\epsilon_r = 0.1$. The fraction of accreted rest mass energy that is returned to the local ISM is then given by $\epsilon_f \epsilon_r = 0.015$. Feedback is modelled such that each black hole contains energy, E_{BH}. At each time step $\epsilon_f \epsilon_r \dot{m}_{accr} c^2$ is added to E_{BH} and, if the black hole has enough energy to heat a set number of particles, in this case $N_{heat} = 1$, then it is allowed to do so, increasing their temperatures by ΔT_{AGN} according to a heating probability

$$P = \frac{E_{BH}}{\Delta \epsilon_{AGN} N_{ngb} \langle m_g \rangle}, \tag{2.16}$$

with N_{ngb} the number of gas neighbours and $\Delta \epsilon_{AGN}$ the change in internal energy per unit mass for the temperature increase assuming primordial, fully ionized gas. The energy of the black hole is then reduced by the expectation value of the injected energy. The temperature increase is set to $\Delta T_{AGN} = 10^{8.5}$K which is higher than for stellar feedback as the gas density around black holes is significantly higher than star forming gas. As a result a higher temperature jump is required for AGN feedback.

2.2.4 Friends-of-Friends

To seed the black holes; apply the subgrid physics; and enable the study of haloes, galaxies including groups and clusters have to be identified and defined. This is done in the simulation using the SUBFIND algorithm from Springel et al. (2001a); Dolag et al. (2009). The first step employed is the use of the Friends-

of-Friends (FoF) algorithm to find parent haloes. This works by using a linking length, set to 0.2 times the mean interparticle separation for dark matter, that adds all particles in range of an initial particle to a group (friends). This is then done for all those particles (friends of friends) creating groups. The gas and star particles are assigned to the same group as their nearest dark matter particle. SUBFIND, which acts on all particle types, then identifies overdense regions within FoF haloes that are bounded by saddle points and removes all unbounded particles creating subhaloes. Finally any subhaloes separated by less than 3 pkpc are merged and very low mass haloes dominated by a single particle are removed. For each FoF halo the subhalo that contains the particle with the lowest gravitational potential is set to be the central galaxy with all other subhalo's defined as satellite galaxies.

2.2.5 Examples of structure formation in EAGLE

Figures 2.2 and 2.3 are examples of the simulation using the methods discussed above. Figure 2.2 shows how the gas, dark matter and star particles evolve over the course of the simulation. The simulation starts at the initial conditions, a near homogeneous universe that is perturbed by a Gaussian random field. This can be seen in the $z = 2.012$ plot which has some structure but still has the dark matter particles largely dispersed and the gas particles even more so. As the simulation runs the dark matter collapses further and further, creating much more defined structures and, as the dark matter collapses, the gas follows. Looking at the top left of each plot one can see the small galaxies overtime clump together forming one large galaxy, in line with hierarchical structure formation.

Figure 2.3 is an example of the haloes identified with SUBFIND. The haloes are stored in a number of files organised by FoF mass, the haloes in figure 2.3 represent those in the first file, or the 235 most massive. The largest can be seen

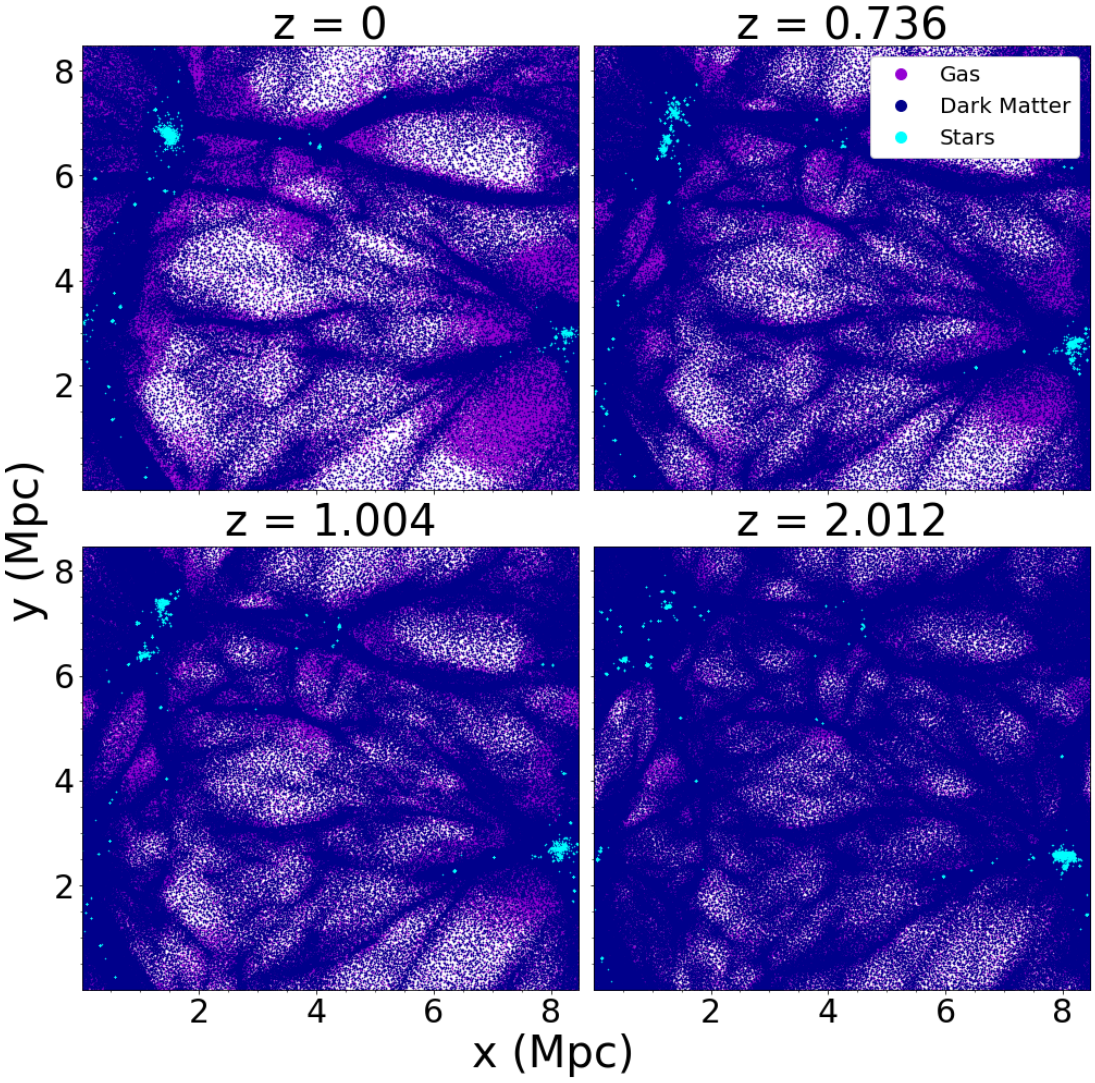

Figure 2.2: From the 12.5 cMpc/h test box of EAGLE simulation, an example of the evolution of dark and baryonic matter over time. The Universe is initially dense but, over time collapses further and further into structures. Note that the axis run from 0 to (12.5 * h)cMpc.

in the centre of the most dense regions of gas while smaller haloes appear along filaments, simulating what is expected for the true Universe.

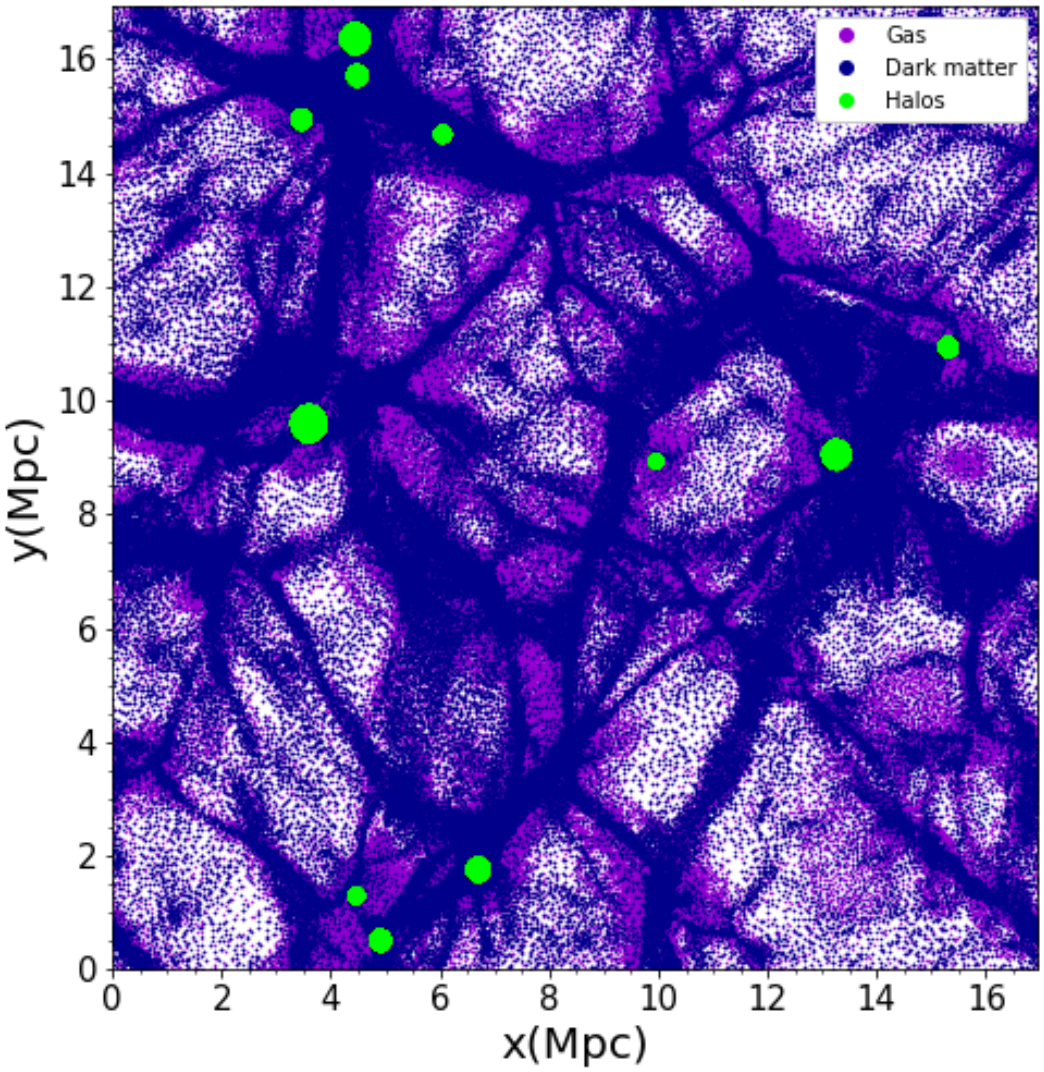

Figure 2.3: The FoF haloes in a 1 Mpc slice of the 25 × 25 Mpc/h box at redshift 0 projected onto a 0.1 Mpc slice (for clarity). The lime points are the baryons (stars and gas) that are within R_{200} of the centre of potential of a group.

2.3 Simulating DMs using sight lines

Using the simulation to simulate a sight line mimicking the path travelled by an FRB, we use a box stacking technique similar to Batten et al. (2021) and originally used by da Silva et al. (2000). The DM is generally dominated by the IGM thus a sight line can be used to find the value of the DM. This was done by picking a random point in a box at a given redshift, randomly selecting a di-

rection and then selecting all gas particles along a square prism across the whole box (as it is periodic). To simulate an FRB whose origin is at a specific redshift, multiple lines are created up to the redshift specified and then stacked together to produce a sight line (a convention of "line" referring to a single prism in a box and "sight line" referring to the stacked total is adopted).

The EAGLE box used in this analysis is the 50 cMpc/h box. While the 100 cMpc/h box is preferable due to the reasons outlined in Batten et al. (2021), memory constraints prohibited its use. To mitigate the effects of the small box size and limited number of snapshots available the location of the line and the direction it travels through the box are randomised. The start point and direction of the lines are generated using the Python Random module that uses the pseudorandom Mersenne Twister algorithm (Matsumoto and Nishimura 1998). The start point is three random floating numbers for x, y, z that are picked outside a 1 cMpc margin of the box to avoid part of a square prism being cut off. The direction is generated as one of three integers that determines the direction of the line, along the x, y or z axis. The square prism in which the particles are selected has dimensions of 10 ckpc $\times$10 ckpc $\times$boxsize (for a line along the z axis).

The side length was chosen to be 10 ckpc as it only has a minor effect on the statistics of the dispersion measure but also minimises the possibility of getting lines without particles in them, which does not represent reality. This is shown in figure 2.4 along with an illustration of the construction of a line. The 3.5 kpc^2 square prism shown in bottom left of figure 2.4 is the statistically converged size according to Batten et al. (2021).

The points in the plot come from a square prism of dimensions 2 cMpc^2 centred on a halo that has been separated into evenly sized smaller square prisms, i.e. for the 200 kpc points (blue) the 2 cMpc^2 square prism is divided into 10 (5×5)

200 kpc^2 square prisms. These smaller square prisms are given the total value of the DM they encompass (so the sum of their DM would be the same as the total DM of the 2 cMpc^2). The pixel fraction on the y-axis is defined as the number of smaller square prisms with a value of DM that sits within a bin divided by the total number of smaller square prisms, e.g. between ($450 <$ DM pc cm^{-3} < 600) there is one of the 200 kpc^2 square prisms thus the pixel fraction would be 1/10. If there are no DM values that fit in a bin then the pixel fraction would be zero. This is why the larger square prisms, such as the 200kpc^2, have more empty bins as they have a lower number of total smaller square prisms. The scatter increases for the larger square prism sizes, as would be expected as there is less granularity in the measure of the DM, but the 75kpc^2 follows the 3.5 kpc data closely, which is a pixel significantly bigger than the 10 kpc one we have used. The potential of having no particles in the line is due to the discrete nature of the particles in the simulation. This potentially could have been alleviated by using the smoothed mass from SPH and remains a potential future improvement.

The "snapshots" for the box only accounts for fixed redshifts of: $0.101; 0.183; 0.271; 0.366; 0.503; 0.615; 0.736; 0.865; 1.004$ up to $z = 1.004$ which, since the boxes are only 50cMpc/h, do not fit together without gaps in the redshift. Thus for stacking, multiple of the same redshift box have been used as an approximation, with the DM contribution of the particles in the sight lines using the true redshift (equation 1.47). This is found by first calculating the redshift of the box e.g. for an FRB at $z = 0.2$, 9,7,1 lines of the $z = 0$, $z = 0.101$, $z = 0.183$ boxes are needed respectively and the final box takes the redshift to $z = 0.202$ (the granularity of a source redshift is 1 box, 50 cMpc/h). Converting distance to redshift was done by first creating a table of redshift to distance in steps of $z = 0.05$ using

$$d = c \int \frac{dz}{h_0 \sqrt{\Omega_m (1+z)^3 + \Omega_\lambda}}. \tag{2.17}$$

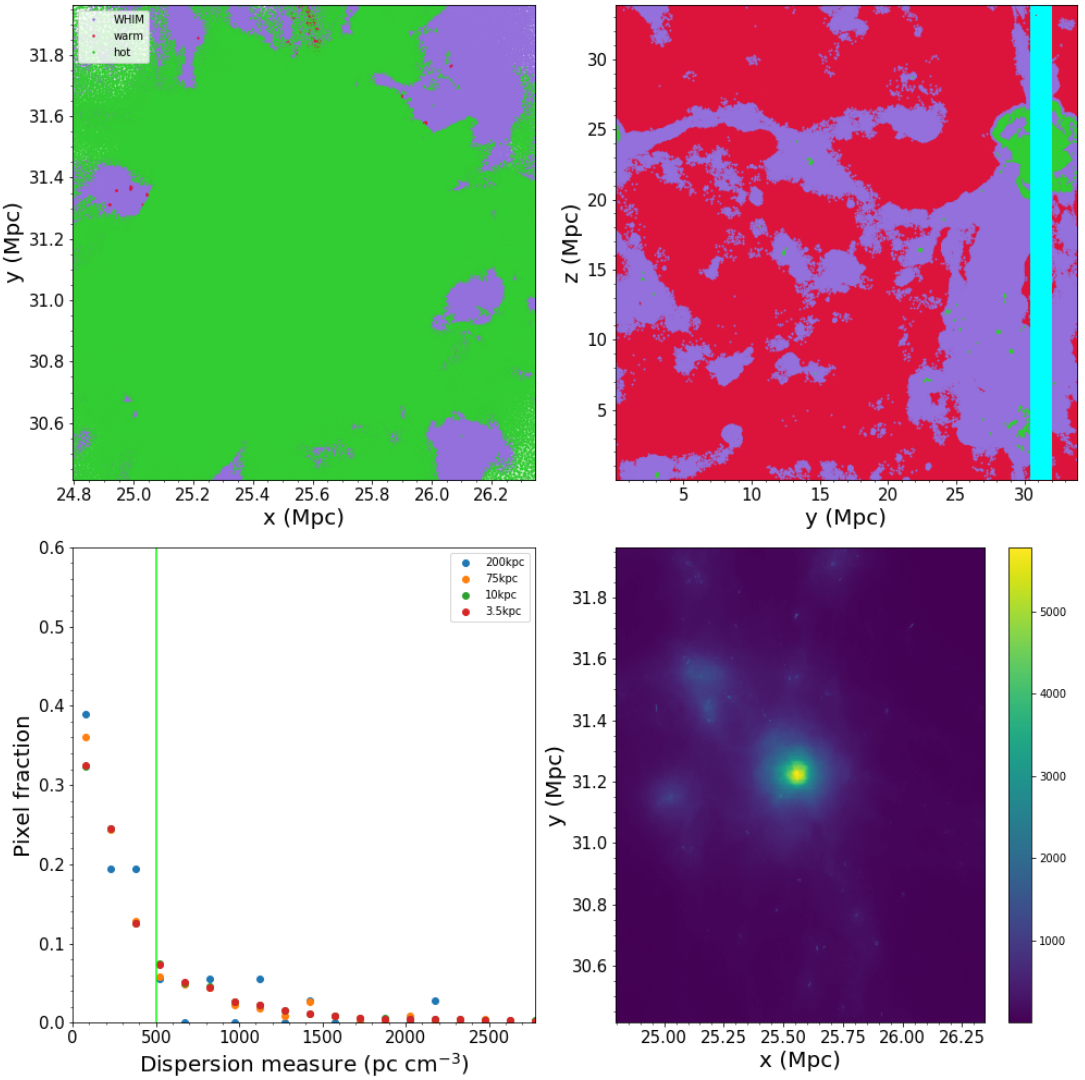

Figure 2.4: The top left plot shows the gas when looking down the line, along the z axis and the top right plot shows the created line in a 1 Mpc slice of the z, y axis, with all plots at $z = 0$. The bottom left shows the effect of changing the square prism size used to divide up a larger 2Mpc^2 square prism. The vertical green line indicates the average DM of the 2Mpc^2 square prism. The bottom right shows looking down (again along the z axis) the 2Mpc^2 square prism divided up using a smaller square prism of size 10kpc^2 (the green points on the bottom left plot) with the colour chart indicating the total DM along the line of each pixel (in pc cm^{-3}). The line travels through a cluster shown in the top right by the abundance of hot gas.

Then the results were used with the scipy module interpolate.interp1d to approximate a function for $z(d)$ by creating straight lines between each point (linear

interpolation).

The redshift of each particle in the line is then calculated by assuming the 0 coordinate is the previously calculated box redshift and the DM from particles can then be scaled based on their distance along the line.

Since electrons are not directly simulated in EAGLE and are what contribute to the DM, the number of them are instead calculated from the gas particles. They are assumed to be fully ionised (which wont hold in the cold dense gas). Using the fact that hydrogen contributes one free electron per nucleon and helium contributes two per four nucleons the mean molecular mass per free electron can be found by $\mu_e = 2/(1+x)$ with the hydrogen mass fraction (the ratio of hydrogen over all gas in the Universe) $x = 0.76$. The DM contribution (as a surface area) of a single particle is then found by

$$DM_{particle} = \frac{m_{particle}}{m_p \mu_e \sigma}(1 + z_{particle}), \tag{2.18}$$

with m the mass of the particle, σ the area of the prism, m_p the proton mass and z the redshift of the particle. The $(1 + z)$ factor comes from the $(1 + z)^2$ from the comoving surface area and the $(1 + z)^{-1}$ from the dispersion measure. The total DM of the stacked sight line is then the sum over all the particles along it, i.e. using a sum to approximate the integral in equation 1.47. The condensed gas of the simulation is omitted from the summation as it is artificially added (since EAGLE lacks the resolution to directly model it accurately) and only makes up a small percentage ($\approx 6 \times 10^{-5}\%$) of the total gas, thus has a negligible effect on the DM of the IGM (but has a much more noticeable effect when looking a collapsed object as in section 3.2.2). To avoid having to create thousands of lines for each individual analysis they have been instead separately created and stored. The lines are made as prescribed above and all the particles within each line are

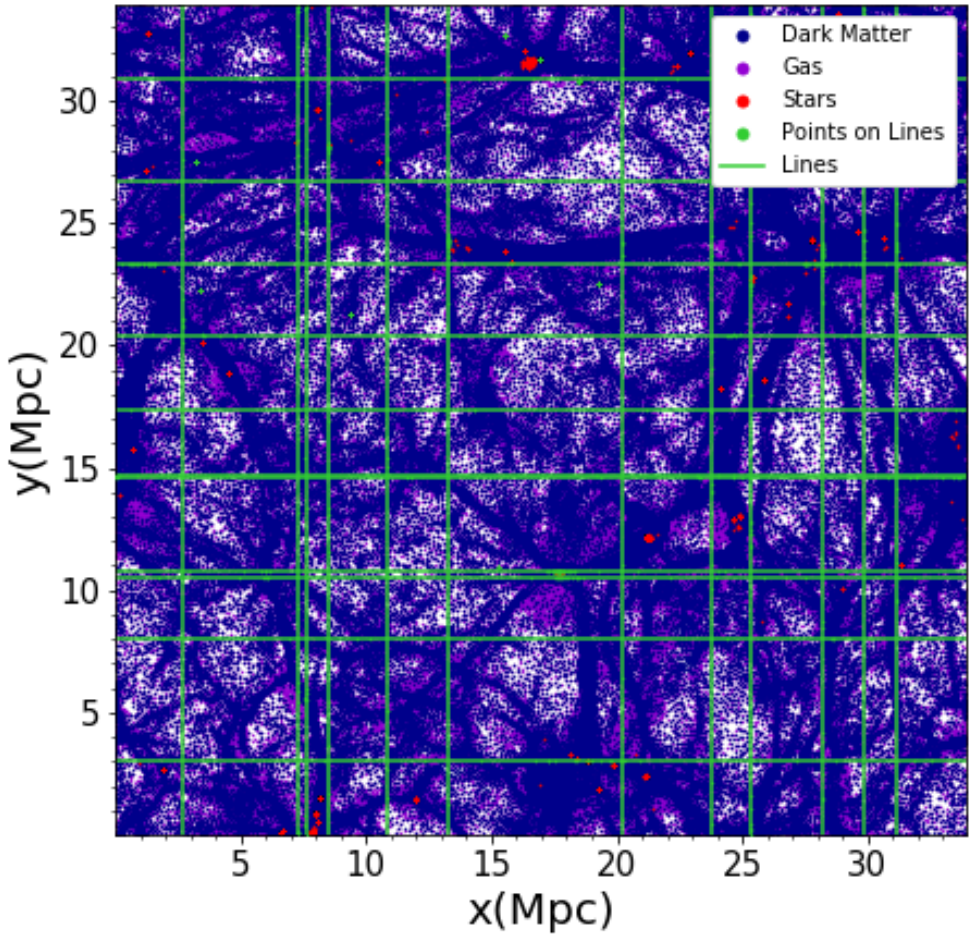

Figure 2.5: 32 generated lines and their associated particles in the centre 0.1 Mpc slice of the 50 Mpc/h box at $z = 0$. Lines that travel along the z axis go into the page thus are only single points on this plot.

stored (shown in figure 2.5) so that if one is needed, it can be called in rather than being constructed during the analysis which adds to computation times. For each of the ten snapshots up to and including $z = 1.004$, 10000 lines have been generated.

Chapter 3

Results

This chapter presents the analysis done using the methods outlined in the previous chapter. In section 3.1 the main result of how the DM-z relation is analysed including a look at the statistics of the distribution and how it compares to observed FRBs. Then, in section 3.2 the analysis on how haloes influence the DM is presented. Finally, the analysis on the different density regions of the gas is given in section 3.3 .

3.1 The Redshift - Dispersion Measure Relation

From the 10000 lines per snapshot generated, 10000 sight lines have been constructed up to $z = 1$ by randomly selecting lines to stack. Their average has been compared to the expected value for a homogeneous universe shown in figure 3.1 (equation 1.54). It should be noted that equation 1.54 assumes that all baryons are able to contribute electrons to the DM, ignoring the fact that some may be locked up in stars and black holes. To maintain a consistent comparison, equation 1.54 is multiplied by the gas/baryon fraction from the simulation. This fraction was found by summing the mass of the gas particles in a box and dividing by the expected baryon mass, $\Omega_b \rho_c$. This was done for each snapshot and the mean value over all nine, 0.9632 ± 0.0006, has been used in the background solution (error is

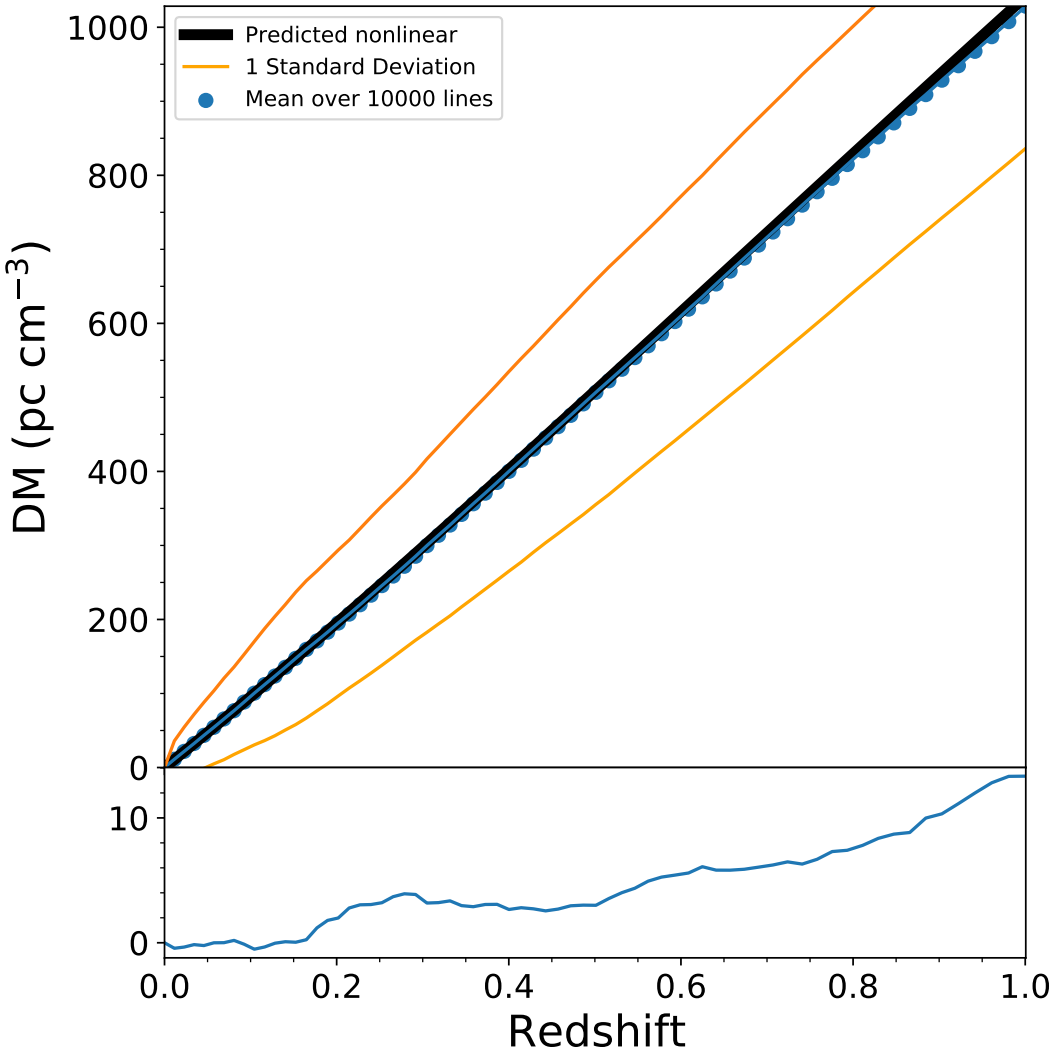

Figure 3.1: The DM-redshift relation with the points from the synthetic sight lines. The black line represents the numerically calculated expected value for a homogeneous universe. The standard deviation is calculated for each point thus, due to the points being cumulative, it is more variable at lower redshifts and smooths out at higher redshifts. The residuals of the results from the simulation compared to the homogeneous universe model are plotted in the bottom panel and show a $\approx 1\%$ discrepancy between the model and the simulation.

the standard error on the mean over the snapshots). The number of boxes used from each snapshot to generate a sight line up to redshift $z = 1$ is $9, 7, 7, 7, 10, 7, 7, 7, 7$ respectively which in practice takes the sight line to redshift $z = 1.004$.

As a crude approximation for the mean DM - z relation a linear model can be made

$$\langle DM_{cosmic} \rangle = az + b, \tag{3.1}$$

which is often cited in the literature as having a zero intercept, $b = 0$. This is since the DM depends only on the number of electrons along its path thus at the origin, since it will not have passed any, it should be zero. The gradient should be positive, reflecting that more electrons are passed with increasing distance. We found that with $b = 0$, $a = 1022 \pm 2$ pc cm^{-3} (errors represent standard errors calculated from scipy.curve_fit) and for a non zero intercept $a = 1039 \pm 2$ pc cm^{-3} , $b = -11 \pm 1$ pc cm^{-3}. This shows that the model must be not linear otherwise it would pass the origin.

This result broadly aligns with other works: Batten et al. (2021) finds $a = 999 \pm 4$ pc cm^{-3}, $b = 17 \pm 6$ pc cm^{-3} and for $b = 0$, $a = 1009 \pm 3$ pc cm^{-3}; Ioka (2003), who uses an analytical model to approximate the DM-z relation using the cosmic baryon density, assumes a homogeneous universe of only hydrogen and finds with $b = 0$, $a \approx 1174$ pc cm^{-3}; Inoue (2004), again using an analytical model, assumes an IGM consisting of 24% helium and the rest fully ionised hydrogen gets a result of, with $b = 0$, $a \approx 960$ pc cm^{-3}. Zhang (2018), using the same method as Inoue (2004) but assumes a 0.875-1 electron baryon ratio and ignores 15% of the baryons, which they state are locked in galaxies, finds a lower value with $b = 0$ of $a \approx 850$ pc cm^{-3}. Zhang et al. (2021), which calculates DMs directly from the electrons in the Illustris simulation, finds $a \approx 892$ pc cm^{-3}. As stated in Batten et al. (2021) linear models are not accurate for low redshifts ($z = 0.5$), instead should be limited as a quick way to compare results.

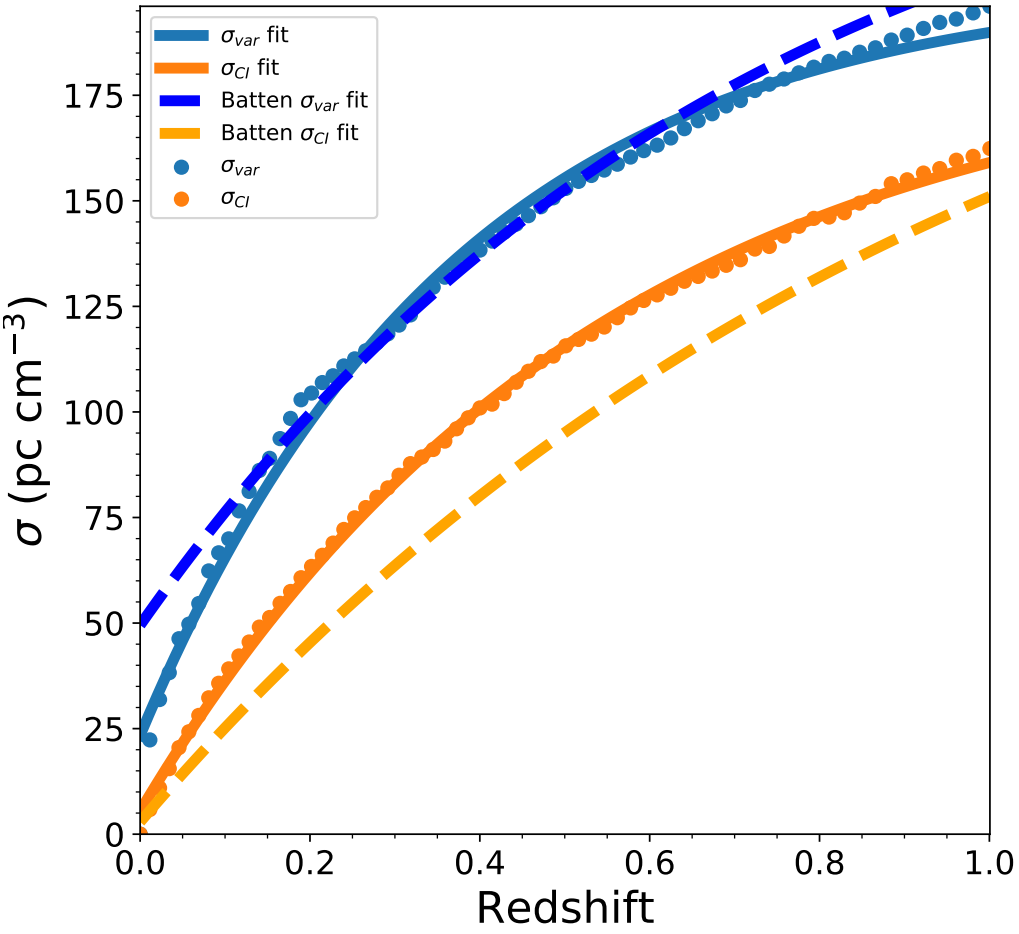

Figure 3.2: The two different definitions of the scatter fitted to exponential models and plotted against the models found by Batten et al. (2021). The points are calculated at the same points as in figure 3.1, i.e. from the cumulative total at the end of each box. The parameters used for the Batten et al. (2021) models are fitted to data from 0 up to $z = 3$ which may contribute to the difference between their models and those found in this analysis but also may be attributed to the number of lines used and the different box sizes used.

3.1.1 The Gaussianity of the Sight Lines

To test how Gaussian the distribution of the DM is for sight lines up to a redshift, two different metrics for the scatter have been used following Batten et al. (2021).

These are given by

$$\sigma^2_{var}(z) = \sum_{i=0}^{Nbins} (DM_i - \langle DM_{cosmic} \rangle)^2 P(DM_i|z) \Delta DM_i, \tag{3.2}$$

$$\sigma^2_{CI}(z) = \left(\frac{DM_{84}(z) - DM_{16}(z)}{2} \right)^2, \tag{3.3}$$

where $P(DM_i|z)$ is the probability that a line of sight has DM_i at redshift z, ΔDM_i is the width of a bin and $DM_{84}(z)$, $DM_{16}(z)$ are the upper and lower respective limits of the 68% confidence interval. σ_{var} is the normal definition of the standard deviation, as plotted in figure 3.1, but σ_{CI} describes the width of the distribution. When the distribution is Gaussian then these are equal but the larger the difference, the less Gaussian the distribution is. An exponential model as a function of redshift can be fit to these metrics

$$\sigma = Ae^{Bz} + C. \tag{3.4}$$

The models and values of σ_{var}, σ_{CI} are plotted along with the models found in Batten et al. (2021) in figure 3.2.

We find values for the parameters as, for σ_{var}: $A = -180 \pm 2$; $B = -2.6 \pm 0.1$; $c = 203 \pm 3$ and for σ_{CI}: $A = -199 \pm 1$; $B = -1.60 \pm 0.03$; $C = 204 \pm 2$. In figure 3.2 it is clear that both the metrics for the scatter are increasing with distance and constitute $\approx 19\%$ for σ_{var} and $\approx 16\%$ for σ_{CI} of the mean at $z = 1$. This may be due to the further distance that is travelled, the more likely the sight line is to pass through a halo which will cause the DM to spike significantly, increasing the scatter. The decreasing of the slope with redshift is because the spike, due to the halo, constitutes less of the total DM thus is not as impactful to the scatter.

Figure 3.2 also shows that the σ_{var} results are very similar to the data found

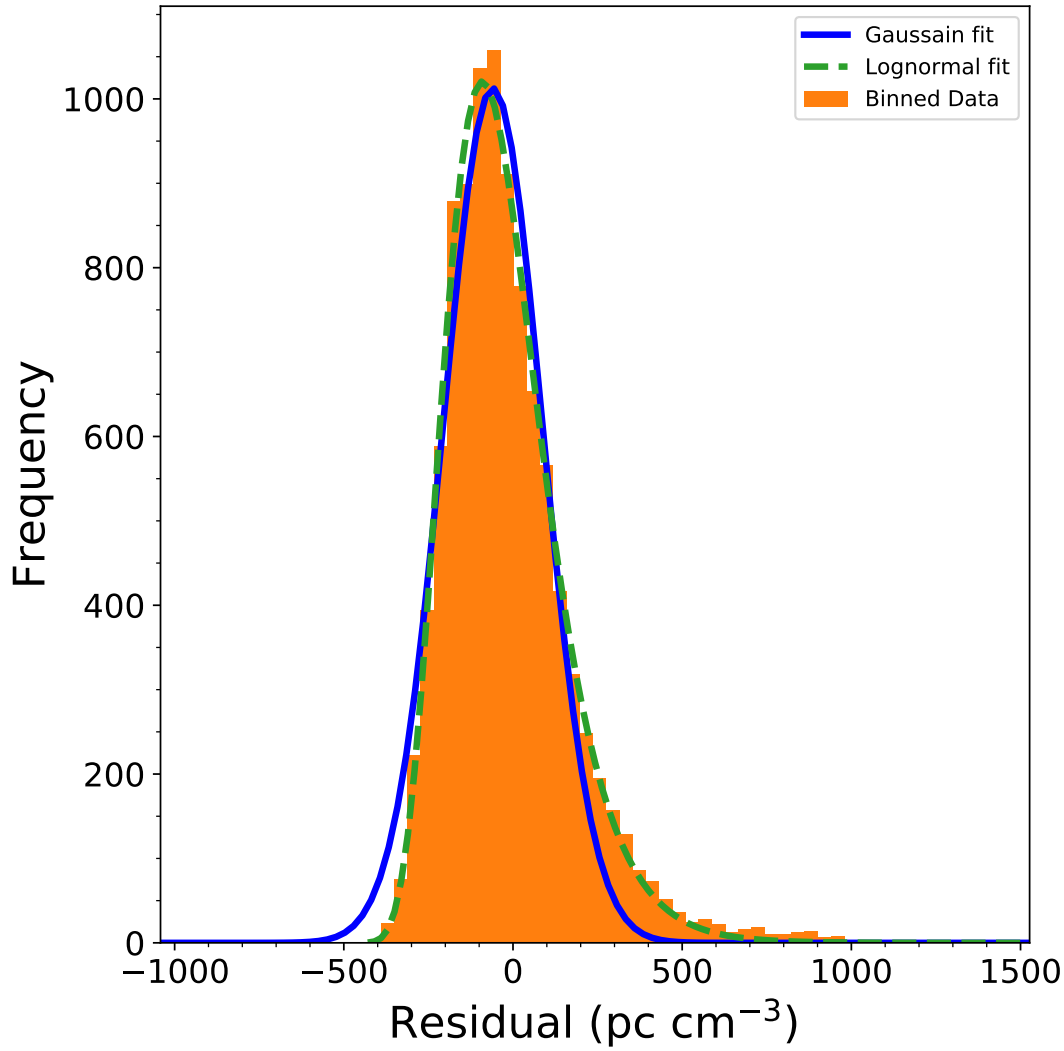

Figure 3.3: At redshift $z = 1$, the residuals of 10000 sight lines (the sum of bins is 10000) binned by how far from the homogeneous solution (equation 1.54) they are. The distribution is skewed towards higher DM values. This is expected since if the sight line passes through galaxies or other collapsed objects the DM will be much higher than the mean.

in Batten et al. (2021) while the σ_{CI} shows a small deviation. The discrepancy in the models is likely due to their models being fitting to data up to $z = 3$, whereas the model we found is fitted from data up to $z = 1$. We end at the same conclusion as Batten et al. (2021), the fit is significantly non Gaussian. To further investigate the nature of the distribution, 10000 sight lines were made

up to $z = 1$ and by how much they deviated from the homogeneous universe solution was binned, shown in figure 3.3. This was then fitted to a Gaussian and log normal model using a Levenberg-Marquardt algorithm with least squares (LevMarLSQFitter from astropy.modeling) for the Gaussian, and a non linear least squares fitter (scipy.curve_fit) for the log normal model. These found, for the Gaussian model: $\sigma = 145.3$ pc cm^{-3}; $\bar{n} = -62.3$ pc cm^{-3} (mean) and for the log normal model: $A = (546 \pm 3) \times 10^3$ (Amplitude); $\sigma = 0.323 \pm 0.009$ pc cm^{-3}; $\bar{n} = 6 \pm 10$ pc cm^{-3}. The total sum of the absolute value of the residuals for each bin of the Gaussian model was found to be 1717.3 and for the log normal model 415.0, a significantly better fit. This can be attributed to the fact that there is a minimum value for the DM representing a sight line through nothing but void. The upper limit, on the other hand, can be much higher than the mean value depending on how many and of what mass haloes the sight line passes through. This plot follows the density distribution of the Universe, as expected since the number of electrons, which make up the DM, is proportional to the mass of the gas travelled through. This is reflected in Coles and Jones (1991) in which a lognormal model is fitted to the distribution of matter in the Universe. Further analysis of how haloes affect the DM is given in section 3.2.

3.1.2 Comparison to Observed Localized FRBs

We compare our results to FRBs of known host galaxies. The FRBs used are shown in table 3.1. The Milky Way and host galaxy contribution to the DM, DM_{MW}, is found in the different reference material differently. Those from Batten et al. (2021) are calculated using NE2001 (Cordes and Lazio 2002), a model/ software for the Galactic distribution of free electrons, whereas those from Macquart et al. (2020) are assumed to be 50 pc cm^{-3}. The Milky Way contribution is subtracted from the observed DM in figure 3.4 for the FRBs as the model we use is for the IGM. There is still the contribution from host galaxies which has

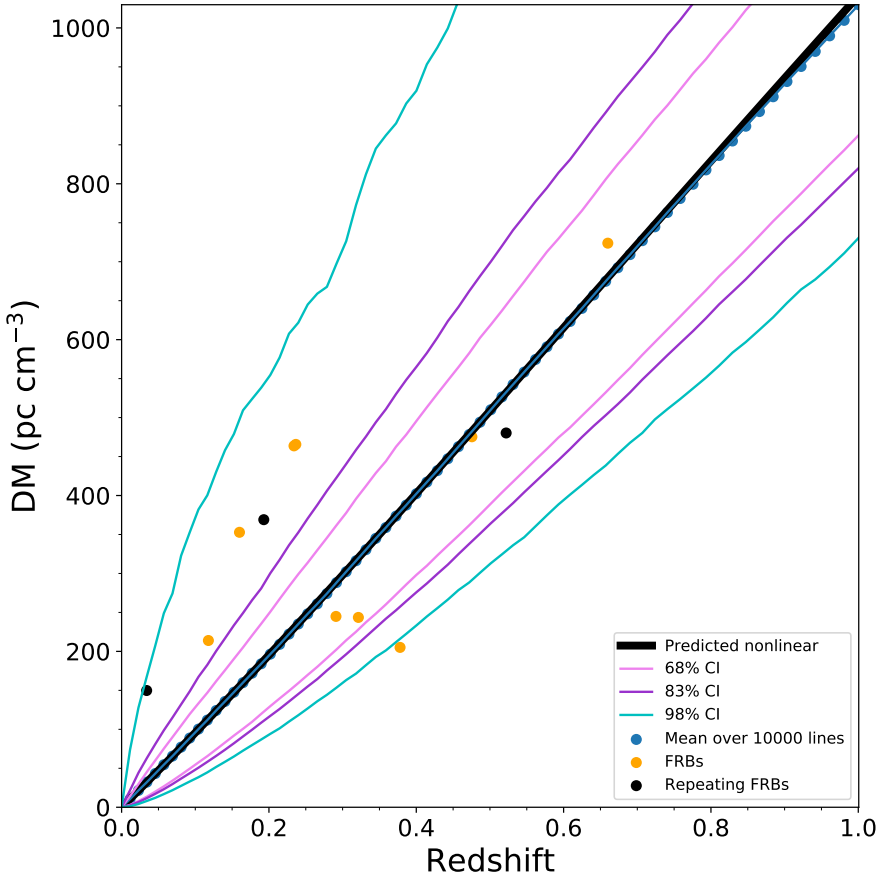

Figure 3.4: The black line is the expected cosmological average for a homogeneous universe multiplied by the baryons in gas fraction (ignoring baryons from stars/ black holes). DM_{cosmic}, and the blue points below the line are those found from the simulation. The lines denoted by CI represent the respective confidence intervals. The low redshift FRBs with higher DM sit above the upper 83% percentile line which may be due to an underestimation of the host galaxy contribution. The lower DM points and those at higher redshift fall close to the mean. FRB 190611, the point at $z = 0.378$, has a large uncertainty in its host galaxy's localisation and a closer but fainter source found may instead be the FRB's associated host galaxy (Macquart et al. 2020). This could explain its position close to the 98% line while the other points of similar redshift lay within the 68% confidence interval.

been assumed to be "not a large contribution" to the DM in Batten et al. (2021) but given an ansatz of $DM_{host} = 50/(1+z)\text{pccm}^{-3}$ in Macquart et al. (2020). We explore the effects of host galaxies in section 3.2.

FRB	DM (pc cm^{-3})	Host z	DM_{MW} (pc cm^{-3})	Source
121102	557.0	0.193	188	Tendulkar et al. (2017)
180916	348.8	0.034	199	Marcote et al. (2020)
180924	361.42	0.3214	80	Macquart et al. (2020)
181112	589.27	0.4755	80	Macquart et al. (2020)
190102	363.6	0.291	80	Macquart et al. (2020)
190523	760.8	0.660	37.0	Ravi et al. (2019)
190608	338.7	0.1178	80	Macquart et al. (2020)
190611	321.4	0.378	80	Macquart et al. (2020)
190711	593.1	0.522	80	Macquart et al. (2020)
190714	504.1	0.2365	38.5	Heintz et al. (2020)
191001	507.9	0.2340	44.2	Bhandari et al. (2020)
200430	380.0	0.160	27.2	Heintz et al. (2020)

Table 3.1: The FRBs of known host origin. Since the DM calculated from the simulation for this comparison is that of the IGM, removing the contribution of the Milky Way will result in a more consistent comparison. This is done differently in the source data and is noted above. Data is as presented in Batten et al. (2021) except for those taken from Macquart et al. (2020).

Shown in figure 3.4 is the observed FRBs plotted with the DM-z relation from 3.1 and three confidence interval lines reflecting the non Gaussianity of the distribution. The observed FRB's at lower redshifts (180916, 190608, 200430, 121102, 191001) sit in between the upper 83% and 98% confidence interval lines. This may be due to an underestimation in the host/Milky Way contribution or, due to the low sample size may be due to these FRBs travelling through either galaxy haloes or overdense regions. The FRBs at higher redshifts follow the average much closer, this can be attributed to the further distance travelled causing the DM to average out, reducing the effects of incident haloes. It should be noted that FRBs: 180916; 121102; 190711 are repeaters. They are included in figure 3.4 but may not have the same progenitor as non-repeaters and could potentially have different properties as yet unknown that affect their DMs.

3.2 The Effect of Galaxies on the DM

3.2.1 Local Effects

For observations the effect the host galaxy and intervening galaxies have on the DM is important, the FRBs in figure 3.4 could have only a small contribution from the host galaxy or could be dominated by it. This could also depend on the type and mass of the host galaxy and the temperature and density of gas within it.

In this section we test: the effects of FRBs with an offset; how the mass of the host halo affects the DM and the assumption that all gas is fully ionised. For examining the effect haloes have on DMs, we created lines that are centred on a halo rather than starting at a random point. These are then used as the final line along a sight line, simulating an FRB that originates from a halo. As before the lines are produced across the length of the box but for the single line analysis (subsection 3.2.1), to avoid the line going through the full width of the halo, the line is cut 2 cMpc short from the end. Since the end (and start) are within the centre of the halo this avoids passing through it twice.

Lines that were centred on all haloes identified by the simulation of mass above $M > 10^{11} M_{\odot}$ were grouped by their halo mass: clusters $M > 10^{14} M_{\odot}$; groups $3 \times 10^{13} M_{\odot} < M < 10^{14} M_{\odot}$; massive galaxies $5 \times 10^{12} M_{\odot} < M < 3 \times 10^{13} M_{\odot}$; galaxies $10^{11} M_{\odot} < M < 5 \times 10^{12} M_{\odot}$ with the mass of the halo defined as the FoF M_{200} mass.

As shown in figure 3.5 the origin of the FRB was then moved a distance from the centre at intervals such that the segment from the halo centre to the new start point was cut out. This simulated the effect on the DM of an FRB that starts further and further away from the centre of its host halo. We have assumed that the gas is fully ionised. This is true for gas of $T > 10^4$K so does not affect the IGM which is almost all above this limit but in haloes, particularly in lower mass

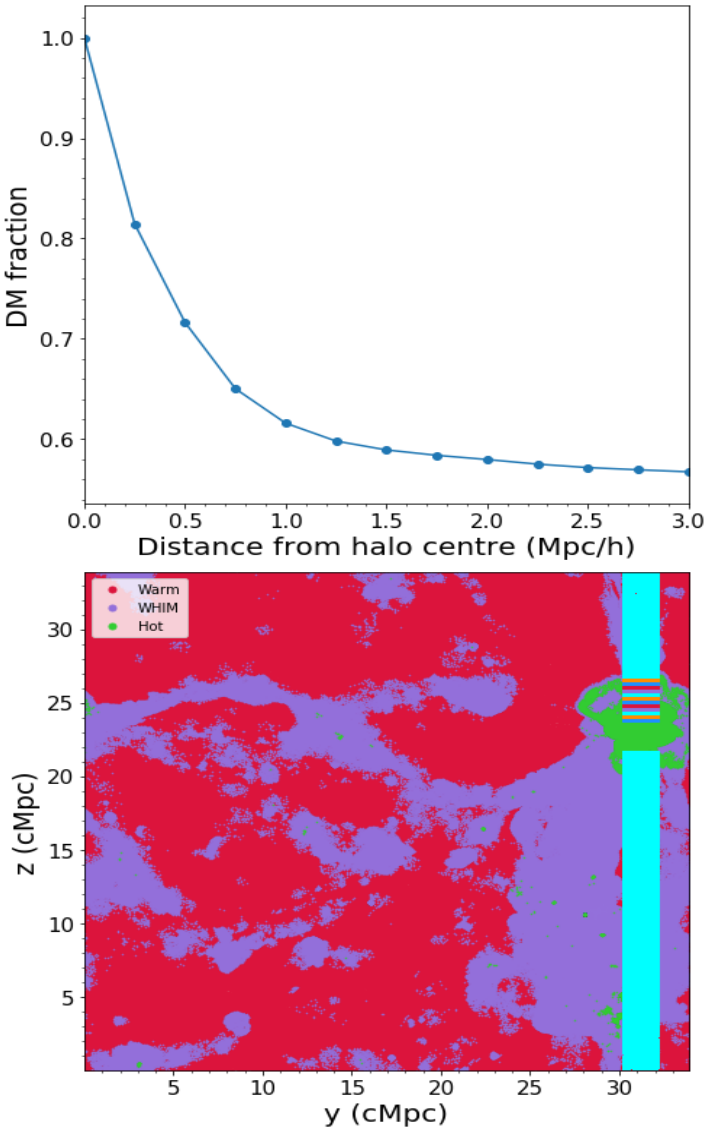

Figure 3.5: An example of the analysis done for figure 3.6 for a single cluster with a 1 cMpc ×1 cMpc line for clarity. The DM fraction on the y axis of the top plot is the ratio of the DM for a line starting a distance from the halo's centre over the DM starting at the halos centre, thus why at 0 Mpc/h the value is one. The different distances from the haloes, simulating FRBs from with different offsets, are indicated on the bottom plot by different coloured lines. The lines are overlapping such that the bottom dark blue line is the point on the left plot at 0 Mpc and the cyan line on top is the final point in the top plot.

galaxies and at higher redshifts, this becomes less true. The make up of haloes by gas phase against halo mass is shown in figure 3.7.

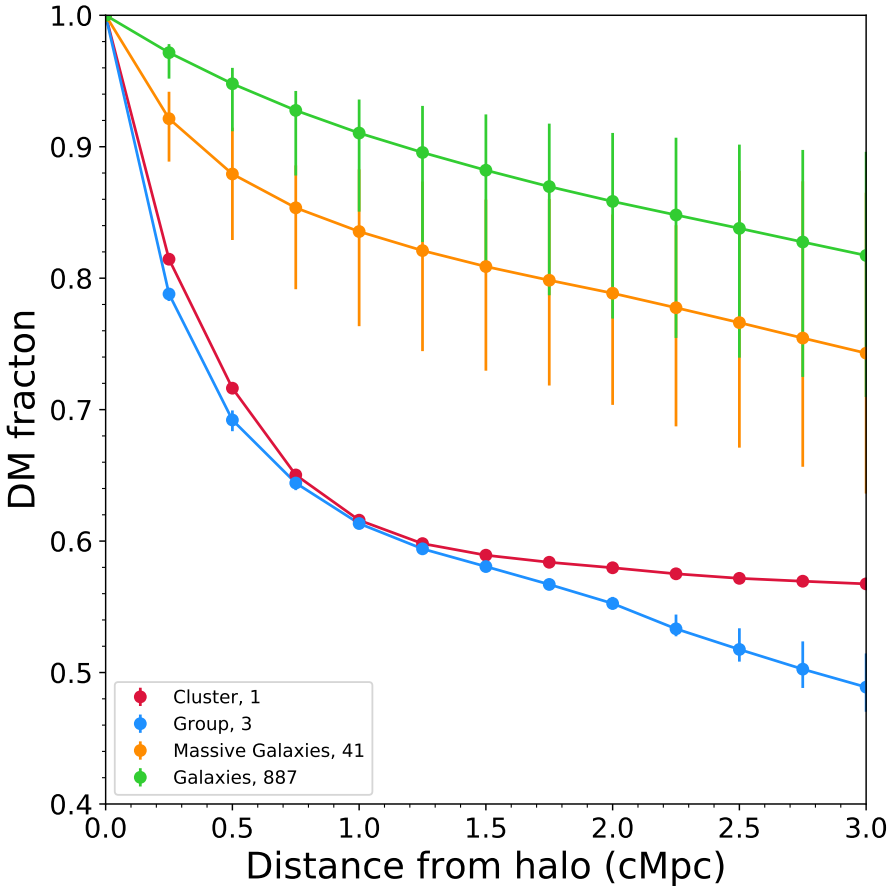

Figure 3.6: The effect of an FRB that originates further and further from the centre of the host galaxy. The lines represent the average values over the objects shown in the legend. The error bars represent the 75 and 25 percentiles of the population thus, since there was only one cluster it has no error bars. The y axis shows the fraction of the DM remaining after cutting the line hence why the fraction is at unity at the halo centre.

The results in figure 3.6 show that an FRB moving further from the centre of its host galaxy has a reduced contribution to the DM, eventually settling to the approximately linear trend. This linear trend is as expected from reducing distance passed through the intergalactic medium as it should be approximately homogeneous. This is expected as the density of gas drops off with radius for a galaxy. Another clear trend is that of the higher mass haloes relative contribution dropping off significantly faster than the lower mass haloes the further

from their centre the FRB is. This can be explained by the fact that the larger halos are far more dense than the surrounding IGM, thus contribute more to the total DM despite also causing the total DM of sight lines centred on them to be significantly higher (later shown in figure 3.9). The radius of the less massive haloes is significantly lower than that of the more massive ones, ≈ 0.05 Mpc for the galaxies, $1-2$ Mpc for the groups, and that all haloes have the same density profile (Navarro et al. 1997). This means that the exponential decay seen in the groups and cluster lines is the same profile in the galaxies and massive galaxies but scaled up due to their larger radius.

Since the analysis only applies up to $z = 1$ the partially ionised gas does not make a large contribution to the clusters and groups, but may have a more noticeable effect on the lower mass galaxies. Figure 3.7 also shows that the fraction of gas in the condensed phase is low, particularly at redshifts $0 < z < 1$. Due to this we have excluded it in the analysis as it does not make a significant difference to the DMs calculated. Stars also make up a larger fraction of the mass in the higher mass haloes. They do not contribute to the DM but this does not constitute enough of an effect to balance the higher mass of the halo contributing more electrons to the FRB as seen in figure 3.8.

3.2.2 The Effect on DMs of Sight Lines Starting at Haloes

The analysis is extended to full sight lines that end at haloes, simulating an FRB from a host galaxy at distances larger than just 50 Mpc/h. Unlike before these lines pass through the whole halo rather than just one half so represent an upper limit on the effect. To study the effect of the mass of the host halo a set of 2×10000 sight lines were constructed such that each sight line was split on the final line, in which one used a random line and the other was centred on a halo. The sight lines start at $z = 0.35$ or $z = 0.65$ and the halo was taken

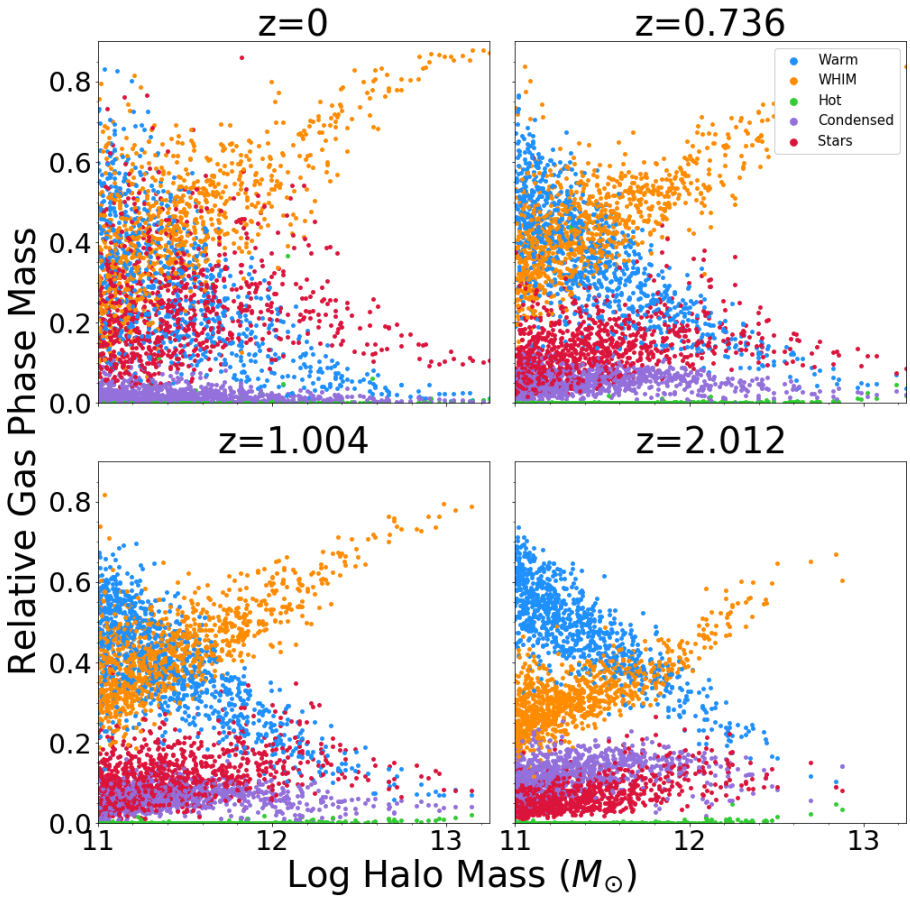

Figure 3.7: The y-axis shows the total mass of each gas phase divided by the total mass of gas in the halo. The x-axis is the mass, M_{200}, of the halo. The haloes plotted are those in the 50 cMpc/h box with mass over $M_{200} > 10^{11} M_\odot$ from four different redshift snapshots. The lower the redshift is the more warm gas there is in larger haloes. Warm gas represents the partially ionised gas thus the assumption of all gas being fully ionised begins to break down in low mass galaxies and galaxies at high redshifts. The gas particles associated with the halo are taken as those within R_{200}.

from the $z = 0.271$ or $z = 0.615$ snapshot. The relative effect, the DM from the sight line ending at the halo divided by the sight line ending at a random point DM_{halo}/DM_{IGM}, was calculated and plotted against the haloes mass shown in figure 3.8. The orange line indicates a linear fit and is of the form

$$\frac{M_{halo}}{DM_{IGM}} = A[\log_{10}(M_{200}/M_\odot) - 11] + B. \tag{3.5}$$

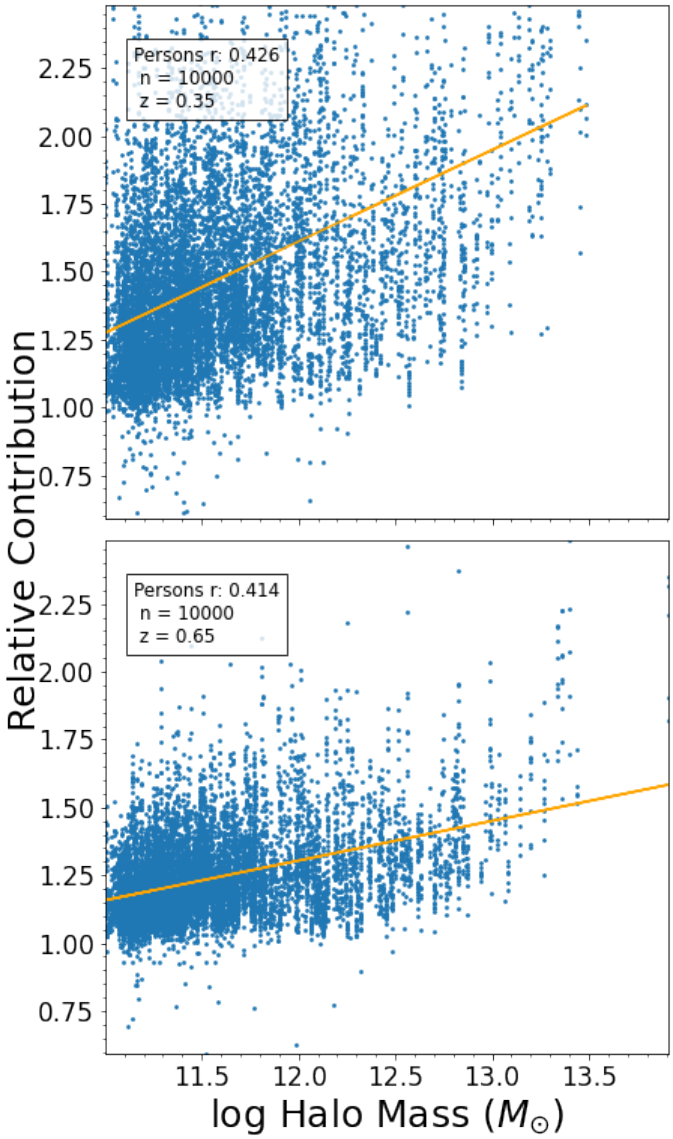

Figure 3.8: The change in contribution for a sight line starting at haloes of different mass at $z = 0.35$, top and $z = 0.65$, bottom. The orange lines represent a linear fit shown in equation 3.5. The y axis represents the DM from the sight line ending in a halo divided by the sight line ending at a random point. The calculated Pearson's r (using scipy.stats.pearsonr) indicates a positive correlation between halo mass and DM contribution.

The constants were found to be, for $z = 0.35$: $A = 0.332 \pm 0.007$; $B = 1.275 \pm 0.005$ and for $z = 0.65$: $A = 0.145 \pm 0.003$; $B = 1.162 \pm 0.002$ with errors calculated

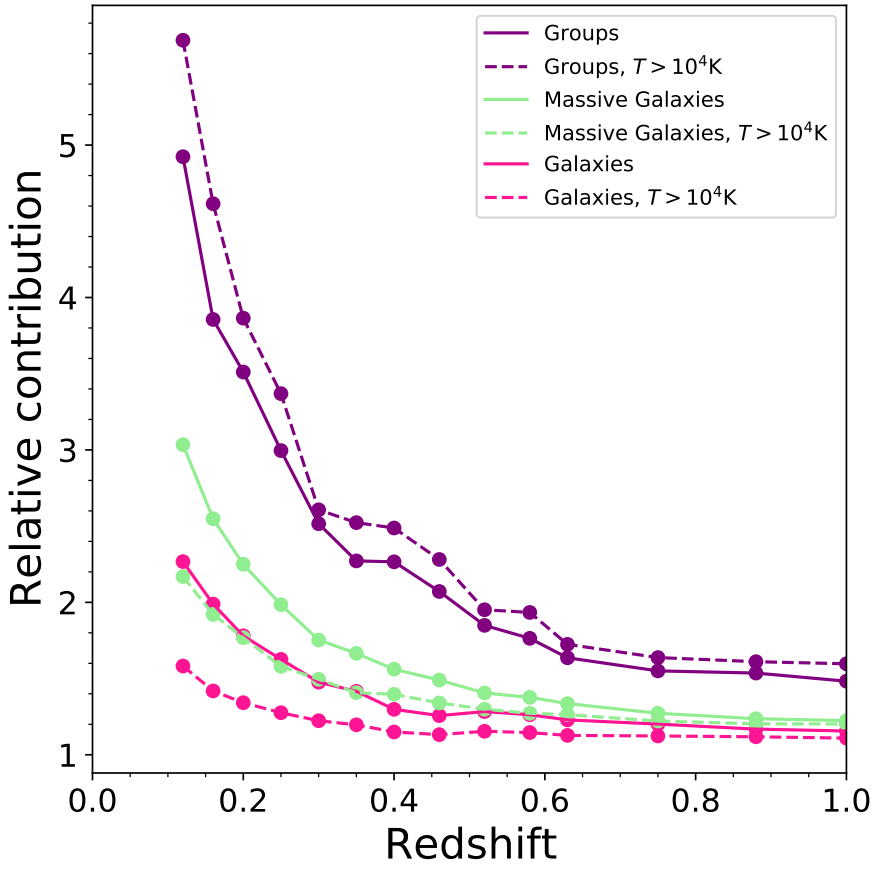

Figure 3.9: The contribution haloes with differing mass have on the DM of an FRB at varying redshift. The dotted line shows the contribution when removing all gas of $T < 10^4$K from the sight line which is where the assumption of the gas being fully ionized begins to break down. This plot agrees with the effect of figure 3.8, that the gap between the contribution from massive haloes and lower mass haloes is greater at lower redshifts and shrinks at larger redshifts.

from standard errors via scipy.curve_fit. The figure shows an increasing trend that is significantly more prevalent at lower redshift likely owing to the fact that at lower redshift the DM is lower overall thus the halo will constitute a larger fraction of the total, particularly the much more massive haloes.

The correlation between halo mass and DM contribution is due to haloes being made almost entirely of gas (excluding dark matter) as shown in figure 3.7 so, having more mass means more gas thus more electrons to contribute to the DM

despite the higher fraction of stars holding electrons. If considering the observed FRBs in table 3.1, FRB 190523's host galaxy is the closest to the simulated redshift of $z = 0.660$ and is a spiral galaxy of mass $10^{11.07} M_{\odot}$. Using the linear fit this galaxy would constitute a 1.17 increase to the DM or 143.3 pccm^{-3}, leaving a cosmic DM of 617.5 pccm^{-3}. This is closer to the cosmic value of 679.6 pccm^{-3}. Considering this is a lower limit from both assuming fully ionised gas and travelling through the entire halo, it can be expected the effect will be significantly smaller. This then combined with the DM contribution from the Milky Way should then result, on average, in DM_{cosmic}.

Finally, the effect of haloes over different redshifts is shown in figure 3.9. For each point 10000 sight lines to the redshift were made, each ending at a halo in one of the categories. The halo type was randomly selected from the lines created thus, since there are much fewer groups than galaxies, significantly less sight lines have been made for them. To avoid too few group sight lines, 10 are forced to start from them. Due to the lack of groups in the boxes some of the sight lines have used duplicate halo lines but with different random lines being stacked to them.

To test if the assumption that all gas is fully ionized is valid, a separate set of sight lines were made excluding all gas with $T < 10^4$K, which is where the assumption is expected to break down. This resulted in a large difference between the fully ionised assumption for galaxies, a moderate difference in massive galaxies and a negative difference for groups. The negative difference in the groups is due to the group itself having less gas at $T < 10^4$K than the IGM thus removing it results in a higher contribution from the groups. This can be seen in figure 3.7 which shows that lower mass galaxies consist of more warm gas (recall $T < 10^5$K) and the more massive galaxies consist of more gas in the WHIM phase ($T > 10^6$K). At low redshifts all types of haloes contribute a much larger effect to

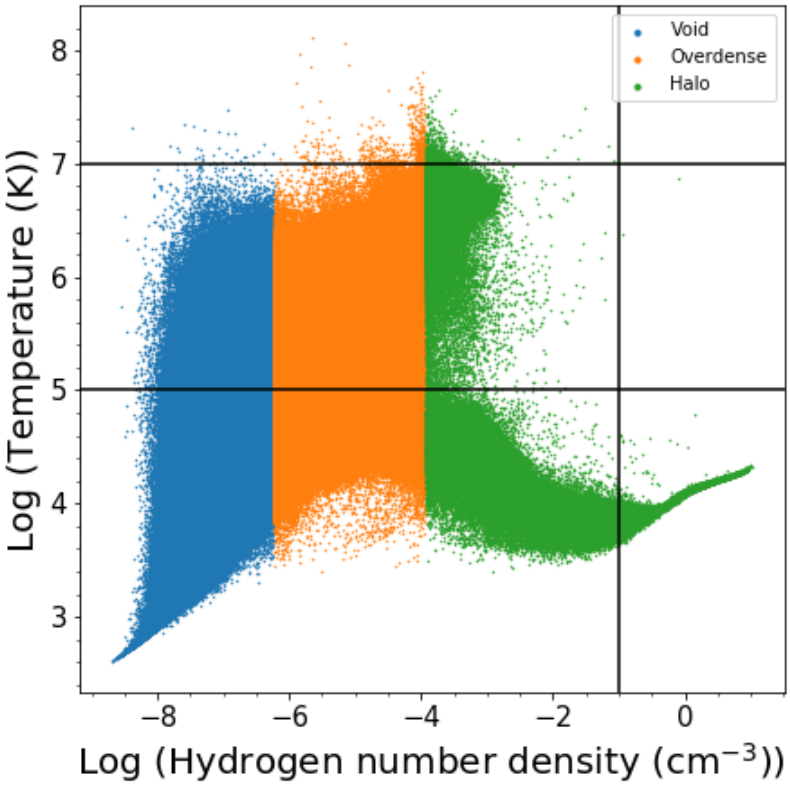

Figure 3.10: All the gas particles within a 1 Mpc slice of the $z = 0$, 50 Mpc/h snapshot. The black lines separate the different gas phases, right of the vertical line is condensed gas (excluded from the analysis), bottom left is the warm gas, middle left is the WHIM, the expected location of the missing baryons, and upper left is the hot gas. The blue orange and green columns represent the void, overdense and halo groups used in the analysis respectively

the overall DM but increasing redshift averages out this effect and is potentially why the lower redshift FRBs in figure 3.4 are further from DM_{cosmic}.

3.3 The Effect of Gas Density on the DM

While haloes have a major effect on the DM, the majority of it comes from the void and overdense gas of the IGM. As introduced in section 1.2 the IGM is not homogeneous, instead it can be separated into regions that have not collapsed

(voids), regions that have collapsed across one axis (sheets), regions that have collapsed across two axes (filaments) and regions that have collapsed across all three axes (haloes). To truly identify these regions in the simulation the tidal tensor must be solved (Bernardeau et al. 2002) but, due to time constraints this has not been done. Instead, particles of different density have been grouped together and their contribution to the overall DM studied. These groups are: void $\rho_V < \Omega_b\rho_c(t_0)(1+z)^3$; overdense $\Omega_b\rho_c(t_0)(1+z)^3 < \rho_{OD} < 200\Omega_b\rho_c(t_0)(1+z)^3$ and haloes $\rho_h > 200\Omega_b\rho_c(t_0)(1+z)^3$ (shown in figure 3.10). The redshift scaling is to account for the expansion of the Universe, which causes the group's definitions to change with redshift.

The contribution of each different group has been plotted in figure 3.11. To do this sight lines were created as described in section 2.3 but, instead of summing the DM from each particle for each box, they first were separated into the groups. The DMs for the particle in each group were then summed for each box resulting in a separated set of DMs for each group. The ratio of the contribution is shown in figure 3.11. It can be seen that the particles in the halo group influence the DM more at lower redshifts while the void group's contribution grows to fill the difference and the overdense group's contribution stays around $DM_{tot}/DM_{OD} \approx 0.7$. This may be attributed to the evolution of structure formation in the Universe. At earlier times the Universe is closer to a homogeneity thus less collapsed objects exist and the void group encompasses more of the Universe.

Another way to find the contributions from just the DM can be found from an equation of the form

$$DM_{cosmic} = Ad_v + Bd_0 + Cd_h, \tag{3.6}$$

in which d_v, d_o, d_h are the distances travelled in the void, overdense and halo

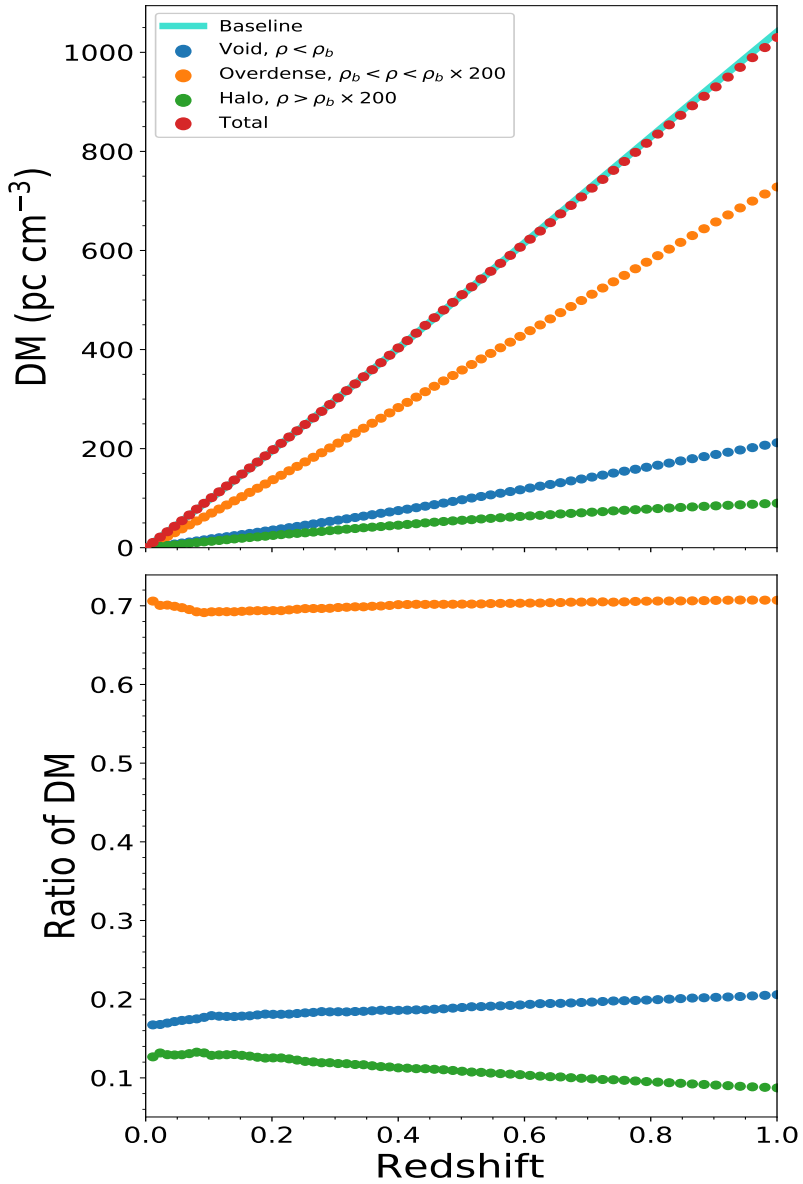

Figure 3.11: Top shows the separated contributions from the different density groups. The total points are the sum of all other points at the redshift. While the halo group on average contributed the least, as shown before they have the potential to influence individual DMs considerably.

groups and A, B, C are constants defined as the average DM per unit distance for each of the groups respectively. Averaging over 10000 sight lines from redshift $z = 1$ these constants were found to be for this simulation $A = 0.16 \pm 0.01$ pc cm^{-3} Mpc^{-1}, $B = 0.8 \pm 0.01$ pc cm^{-3} Mpc^{-1}, $C = 200 \pm 400$ pc cm^{-3} Mpc^{-1}

with the errors representing one standard deviation of the scatter over the sight lines.

These may not be representative of the true values for the Universe and future testing of observed FRBs with there entire path known would be required to compare to these results. The average distance travelled through each group was found by starting at zero in the direction the line travels in, then the first particle reached along the line would determine the group being travelled through. This stops when the next particle is reached which, if part of a different group, would then travel through that group till the next particle. This continues for all the particles along the line. The total distance travelled through all the groups will be the same as the total distance as the last particle in a line is measured through the periodic boundary, i.e until it reaches the first particle. The distances were found to be: 1340 ± 60Mpc for the void; 970 ± 60Mpc for the overdense group and 0.5 ± 0.8Mpc for the halo group (errors represent one standard deviation of the scatter). Combining equation 3.6 with the fact that the distances must sum to a potentially known total, $d_{tot} = d_v + d_o + d_h$ one finds a set of simultaneous equations

$$d_v(A - C) + d_o(B - C) = DM_{cosmic} - Cd_{tot} \tag{3.7}$$

$$d_v(A - B) + d_h(C - B) = DM_{cosmic} - Bd_{tot} \tag{3.8}$$

$$d_o(B - A) + d_h(C - A) = DM_{cosmic} - Ad_{tot}, \tag{3.9}$$

which can be solved to find the average distances travelled through each group given the distance to the FRB and the value of DM_{cosmic}.

To further investigate what particular gas overdensities affect the value of the DM a histogram was made that, similar to figure 3.11, binned the different DM

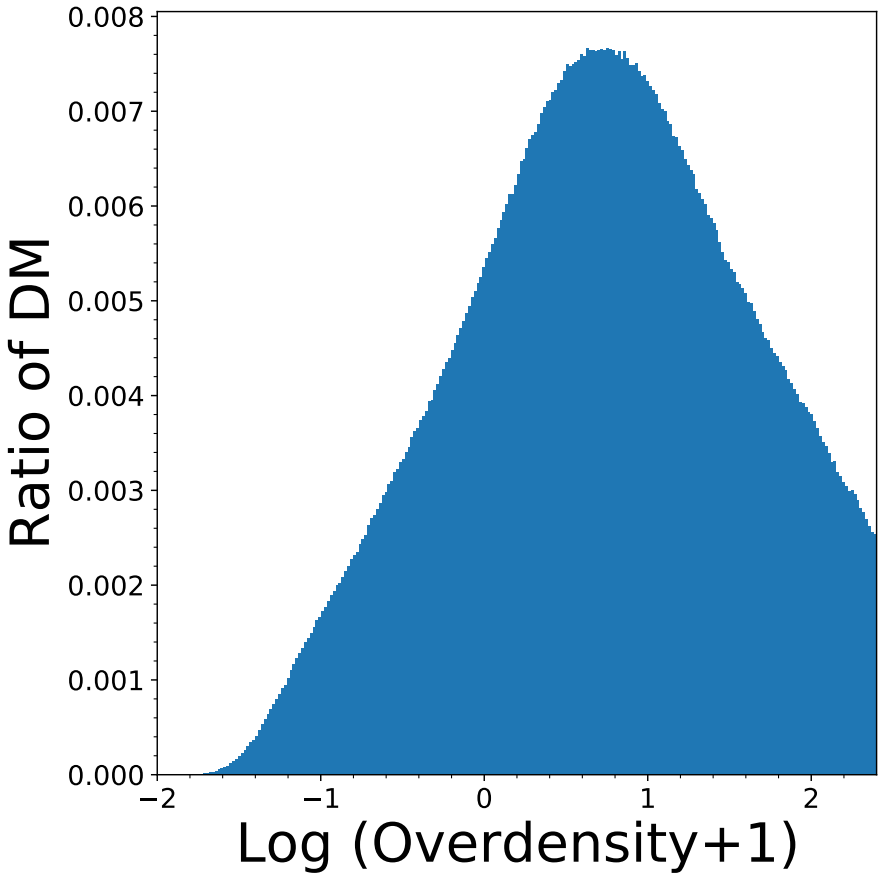

Figure 3.12: The binned average contribution from gas of different densities for 10000 sight lines up to redshift $z = 0.615$. The underdense gas is represented on the x axis as $-2 < \log_{10}(\delta + 1) < 0$. As in figure 3.11 overdense gas, particularly at the lower end of the density group, dominates the contribution.

contributions by gas particle overdensity (figure 3.12). 10000 sight lines were created up to a fixed redshift of 0.615. For each sight line the DM from each overdensity bin was summed such that the area under the full histogram is equal to the total DM.

As was seen in figure 3.11 the moderately overdense gas, $\approx 0.5 < \log_{10}(\delta+1) < 1$, contributes the most to the DM due to a combination of its abundance and higher electron density. While the underdense gas, $\log_{10}(\delta + 1) < 0$, by volume covers most of the sight line's path due to its low density it still contributes

less to the DM than the overdense material. The significantly overdense gas, $\log_{10}(\delta + 1) > 2$, has the opposite effect. It instead has a high electron density but covering a far smaller area of the sight line's path again resulting in a lower contribution to the total DM than the overdense gas.

Chapter 4

Summary and Conclusion

4.1 Summary

In this thesis, the results of the analysis on simulated fast radio bursts (FRBs) using the Evolution and Assembly of GaLaxies and their Environments (EAGLE) simulation has been presented. With a box stacking technique, sight lines have been used to probe the statistics of dispersion measures (DMs), giving insight into how the simulation's intergalactic medium (IGM) behaves, how it compares to observed FRBs and gives either an indication of what future observations may produce or, if future data disagrees, highlights the shortcomings of the simulation. It has been shown that the warm hot intergalactic medium (WHIM) makes a large contribution to the dispersion measure and the average DM follows the cosmological average. This proves the use of DMs from FRBs for detecting the missing baryons which, in the simulation have all been accounted for.

The core issue of a host halo's contribution to the DM was found for the simulation. In particular: how the different types of host halos; their mass; and the FRB's offset contribute to the DM. It was found that at lower redshift, halos contribute a significant amount to the overall DM but, as the distance and DM

increases the contribution decreases. It was also found that the higher the host halo mass, the larger the contribution but also the faster the DM drops off at larger offsets from the centre was. Another result from the analysis was that the partially ionised gas may affect results from lower mass galaxies but not groups. This is due to them being hotter and higher density thus containing fully ionized gas.

How the different densities of gas in the IGM contribute to the DM was then explored. When separating the gas into three groups by overdensity it was found that the "overdense" group contributed the most, the "halo" group contributed the least and dropped off with distance, and that the "void" group's contribution increased over distance. The average distance travelled in each group was found and used to calculate constants that could be used to find, for a given DM of known host redshift, the expected distance travelled through each group and the expected DM contribution of each group. Finally the density groups were separated into density bins leading to an exponential drop off in DM contribution against overdensity.

4.2 Future Work

Time constraints limited the scope of the analysis presented in this thesis. Had there been more time a number of different improvements could have been made. These include: using the 100 Mpc box instead of the 50 Mpc; using the smoothed mass rather than just the discrete particles; using more than 10000 sight lines for improved statistics; not assuming all gas was ionised/ including partially ionised gas; and having more massive halos.

As stated in Batten et al. (2021) the smaller box size causes some repeating structure. This has been mitigated somewhat by use of a random start point and

a random direction but the 100 Mpc box would still be preferable in tandem with these methods for the best result. Using the bigger box will also increase the number of groups and clusters found as they have more space to form enabling better study of these objects. This can be improved further with future simulations that have even large box sizes.

Using the discrete particles should not affect the sight lines as the large distances average out the effect. It is in the single lines which the effect will be more pronounced and would result in a smoother, more realistic value for the total mass along the line. Using the smoothed particles is also consistent with the smoothed particle hydrodynamics (SPH) approach where the gas is instead an average at each point.

As with any population, more is better for statistical analysis and while 10000 sight lines are in line with the results from Batten et al. (2021) who used 1 billion lines, with the potential exception of the σ_{CI} model, more is generally going to be better.

The assumption that all gas in the Universe is fully ionized is reasonable when examining the IGM. It is when considering galaxies and other collapsed objects, especially at higher redshifts, the assumption begins to break down. This is important when considering FRBs are expected to originate from within galaxies. This assumption ideally would be dropped in favour of using some form of model for the number of free electrons from the gas, such as that used by the spectral synthesis code CLOUDY (Ferland et al. 1998).

While the missing baryon problem may be solved within simulations, observations are required to either prove them right, or highlight some of their shortcomings. As of yet only a few have been conducted with limited scope (Nicastro

et al. 2018; Tanimura et al. 2020; Macquart et al. 2020) but, as more observations are carried out (Nandra et al. 2013), the overall trends in their results will get progressively more constrained and locate the missing baryons to a high degree of confidence. For FRBs in particular, as more are discovered, more statistically significant comparisons to the results of the cosmological model can be made. However, it must be considered that with the current unknown origins of FRBs, it may be found that they are unsuitable as cosmological probes thus a better understanding of this would also improve confidence within their results. Future measurements from wide-field interferometers such as CHIME, ASKAP and MeerKAT will continue to add to the total number of FRBs, particularly to the total number with constrained distances required for this analysis (Rafiei-Ravandi et al. 2021; Qiu et al. 2019; Rajwade et al. 2021). As more FRBs are found the better they become for testing cosmological models.

DMs from FRB certainly can act as good cosmological probes, specifically for investigating the nature of gas in the IGM and the general statistics of the Universe. All that remains is to get a statistically significant population of FRBs localised and move from simulations to observations.

References

O. Agertz et al. Fundamental differences between SPH and grid methods. *MNRAS*, 380(3):963–978, Sept. 2007. doi: 10.1111/j.1365-2966.2007.12183.x.

J. Barnes and P. Hut. A hierarchical 0(N log N) force-calculation algorithm. *Nature*, 324(4):446–449, Dec. 1986.

A. J. Batten, A. R. Duffy, N. A. Wijers, V. Gupta, C. Flynn, J. Schaye, and E. Ryan-Weber. The cosmic dispersion measure in the EAGLE simulations. *MNRAS*, 505(4):5356–5369, Aug. 2021. doi: 10.1093/mnras/stab1528.

J. Bergeat and L. Chevallier. The mass loss of C-rich giants. *A&A*, 429:235–246, Jan. 2005. doi: 10.1051/0004-6361:20041280.

F. Bernardeau, S. Colombi, E. Gaztañaga, and R. Scoccimarro. Large-scale structure of the Universe and cosmological perturbation theory. *Phys. Rep.*, 367 (1-3):1–248, Sept. 2002. doi: 10.1016/S0370-1573(02)00135-7.

S. Bhandari et al. Limits on Precursor and Afterglow Radio Emission from a Fast Radio Burst in a Star-forming Galaxy. *ApJL*, 901(2):L20, Oct. 2020. doi: 10.3847/2041-8213/abb462.

M. Birkinshaw. The Sunyaev-Zel'dovich effect. *Phys. Rep.*, 310(2-3):97–195, Mar. 1999. doi: 10.1016/S0370-1573(98)00080-5.

R. G. Bower, A. J. Benson, R. Malbon, J. C. Helly, C. S. Frenk, C. M. Baugh, S. Cole, and C. G. Lacey. Breaking the hierarchy of galaxy formation. *MNRAS*, 370(2):645–655, Aug. 2006. doi: 10.1111/j.1365-2966.2006.10519.x.

R. Cen and J. P. Ostriker. Where Are the Baryons? *ApJ*, 514(1):1–6, Mar. 1999. doi: 10.1086/306949.

S. Chatterjee et al. A direct localization of a fast radio burst and its host. *Nature*, 541(7635):58–61, Jan. 2017. doi: 10.1038/nature20797.

P. Coles and B. Jones. A lognormal model for the cosmological mass distribution.

MNRAS, 248:1–13, Jan. 1991. doi: 10.1093/mnras/248.1.1.

J. M. Cordes and T. J. W. Lazio. NE2001.I. A New Model for the Galactic Distribution of Free Electrons and its Fluctuations. *arXiv e-prints*, art. astro-ph/0207156, July 2002.

L. Cullen and W. Dehnen. Inviscid smoothed particle hydrodynamics. *MNRAS*, 408(2):669–683, Oct. 2010. doi: 10.1111/j.1365-2966.2010.17158.x.

A. C. da Silva, D. Barbosa, A. R. Liddle, and P. A. Thomas. Hydrodynamical simulations of the Sunyaev-Zel'dovich effect. *MNRAS*, 317(1):37–44, Sept. 2000. doi: 10.1046/j.1365-8711.2000.03553.x.

C. Dalla Vecchia and J. Schaye. Simulating galactic outflows with thermal supernova feedback. *MNRAS*, 426(1):140–158, Oct. 2012. doi: 10.1111/j.1365-2966.2012.21704.x.

R. Davé, R. Cen, J. P. Ostriker, G. L. Bryan, L. Hernquist, N. Katz, D. H. Weinberg, M. L. Norman, and B. O'Shea. Baryons in the Warm-Hot Intergalactic Medium. *ApJ*, 552(2):473–483, May 2001. doi: 10.1086/320548.

A. Dey et al. Overview of the DESI Legacy Imaging Surveys. *AJ*, 157(5):168, May 2019. doi: 10.3847/1538-3881/ab089d.

K. Dolag, S. Borgani, G. Murante, and V. Springel. Substructures in hydrodynamical cluster simulations. *MNRAS*, 399(2):497–514, Oct. 2009. doi: 10.1111/j.1365-2966.2009.15034.x.

Euclid Collaboration et al. Euclid preparation: IX. EuclidEmulator2 - power spectrum emulation with massive neutrinos and self-consistent dark energy perturbations. *MNRAS*, 505(2):2840–2869, Aug. 2021. doi: 10.1093/mnras/stab1366.

G. J. Ferland, K. T. Korista, D. A. Verner, J. W. Ferguson, J. B. Kingdon, and E. M. Verner. CLOUDY 90: Numerical Simulation of Plasmas and Their Spectra. *Public. of the Astron. Soc. Pac.*, 110(749):761–778, July 1998. doi: 10.1086/316190.

M. Fukugita. Cosmic Matter Distribution: Cosmic Baryon Budget Revisited. In S. Ryder, D. Pisano, M. Walker, and K. Freeman, editors, *Dark Matter in Galaxies*, volume 220, page 227, July 2004.

R. Genzel et al. A study of the gas-star formation relation over cosmic time. *MNRAS*, 407(4):2091–2108, Oct. 2010. doi: 10.1111/j.1365-2966.2010.16969.x.

R. A. Gingold and J. J. Monaghan. Smoothed particle hydrodynamics: theory and application to non-spherical stars. *MNRAS*, 181:375–389, Nov. 1977. doi: 10.1093/mnras/181.3.375.

F. Haardt and P. Madau. Modelling the UV/X-ray cosmic background with CUBA. In D. M. Neumann and J. T. V. Tran, editors, *Clusters of Galaxies and the High Redshift Universe Observed in X-rays*, page 64, Jan. 2001.

K. E. Heintz et al. Host Galaxy Properties and Offset Distributions of Fast Radio Bursts: Implications for Their Progenitors. *ApJ*, 903(2):152, Nov. 2020. doi: 10.3847/1538-4357/abb6fb.

P. F. Hopkins. A general class of Lagrangian smoothed particle hydrodynamics methods and implications for fluid mixing problems. *MNRAS*, 428(4):2840–2856, Feb. 2013. doi: 10.1093/mnras/sts210.

S. Inoue. Probing the cosmic reionization history and local environment of gamma-ray bursts through radio dispersion. *MNRAS*, 348(3):999–1008, Mar. 2004. doi: 10.1111/j.1365-2966.2004.07359.x.

K. Ioka. The Cosmic Dispersion Measure from Gamma-Ray Burst Afterglows: Probing the Reionization History and the Burst Environment. *ApJL*, 598(2): L79–L82, Dec. 2003. doi: 10.1086/380598.

A. Jenkins. A new way of setting the phases for cosmological multiscale Gaussian initial conditions. *MNRAS*, 434(3):2094–2120, Sept. 2013. doi: 10.1093/mnras/stt1154.

J. Kennicutt, Robert C. The Global Schmidt Law in Star-forming Galaxies. *ApJ*, 498(2):541–552, May 1998. doi: 10.1086/305588.

B. Kocsis and A. Loeb. Menus for Feeding Black Holes. *Space Sci. Rev.*, 183 (1-4):163–187, Sept. 2014. doi: 10.1007/s11214-013-0015-5.

E. Komatsu et al. Seven-year Wilkinson Microwave Anisotropy Probe (WMAP) Observations: Cosmological Interpretation. *ApJS*, 192(2):18, Feb. 2011. doi: 10.1088/0067-0049/192/2/18.

J. H. Krolik and T. Di Matteo. Active Galactic Nuclei: From the Central Black Hole to the Galactic Environment. *American Journal of Physics*, 68(5):489–489, May 2000. doi: 10.1119/1.19463.

G. Liu, J. Koda, D. Calzetti, M. Fukuhara, and R. Momose. The Super-linear Slope of the Spatially Resolved Star Formation Law in NGC 3521 and NGC

5194 (M51a). *ApJ*, 735(1):63, July 2011. doi: 10.1088/0004-637X/735/1/63.

J. P. Macquart et al. A census of baryons in the Universe from localized fast radio bursts. *Nature*, 581(7809):391–395, May 2020. doi: 10.1038/s41586-020-2300-2.

B. Marcote, K. Nimmo, J. W. T. Hessels, S. P. Tendulkar, C. G. Bassa, et al. A repeating fast radio burst source localized to a nearby spiral galaxy. *Nature*, 577(7789):190–194, Jan. 2020. doi: 10.1038/s41586-019-1866-z.

M. Matsumoto and T. Nishimura. Mersenne twister: a 623-dimensionally equidistributed uniform pseudo-random number generator. *ACM Transactions on Modeling and Computer Simulation*, 8(1):3–30, Jan. 1998. doi: 10.1145/272991.272995.

M. McQuinn. Locating the "Missing" Baryons with Extragalactic Dispersion Measure Estimates. *ApJL*, 780(2):L33, Jan. 2014. doi: 10.1088/2041-8205/780/2/L33.

B. D. Metzger, E. Berger, and B. Margalit. Millisecond Magnetar Birth Connects FRB 121102 to Superluminous Supernovae and Long-duration Gamma-Ray Bursts. *ApJ*, 841(1):14, May 2017. doi: 10.3847/1538-4357/aa633d.

K. Nandra et al. The Hot and Energetic Universe: A White Paper presenting the science theme motivating the Athena+ mission. *arXiv e-prints*, art. arXiv:1306.2307, June 2013.

J. F. Navarro, C. S. Frenk, and S. D. M. White. A Universal Density Profile from Hierarchical Clustering. *ApJ*, 490(2):493–508, Dec. 1997. doi: 10.1086/304888.

F. Nicastro, J. Kaastra, Y. Krongold, S. Borgani, E. Branchini, et al. Observations of the missing baryons in the warm-hot intergalactic medium. *Nature*, 558 (7710):406–409, June 2018. doi: 10.1038/s41586-018-0204-1.

R. Perna and A. Loeb. X-Ray Absorption by the Hot Intergalactic Medium. *ApJL*, 503(2):L135–L138, Aug. 1998. doi: 10.1086/311544.

E. Petroff, J. W. T. Hessels, and D. R. Lorimer. Fast radio bursts. *A&AR*, 27 (1):4, May 2019. doi: 10.1007/s00159-019-0116-6.

Planck Collaboration et al. Planck 2013 results. I. Overview of products and scientific results. *A&A*, 571:A1, Nov. 2014. doi: 10.1051/0004-6361/201321529.

Planck Collaboration et al. Planck 2018 results. I. Overview and the cosmological legacy of Planck. *A&A*, 641:A1, Sept. 2020a. doi: 10.1051/0004-6361/201833880.

Planck Collaboration et al. Planck 2018 results. VI. Cosmological parameters. *A&A*, 641:A6, Sept. 2020b. doi: 10.1051/0004-6361/201833910.

D. J. Price. Modelling discontinuities and Kelvin Helmholtz instabilities in SPH. *Journal of Computational Physics*, 227(24):10040–10057, Dec. 2008. doi: 10.1016/j.jcp.2008.08.011.

H. Qiu, K. W. Bannister, R. M. Shannon, T. Murphy, S. Bhandari, D. Agarwal, D. R. Lorimer, and J. D. Bunton. A survey of the Galactic plane for dispersed radio pulses with the Australian Square Kilometre Array Pathfinder. *MNRAS*, 486(1):166–174, June 2019. doi: 10.1093/mnras/stz748.

M. Rafiei-Ravandi, K. M. Smith, D. Li, et al. CHIME/FRB Catalog 1 Results: Statistical Cross-correlations with Large-scale Structure. *ApJ*, 922(1):42, Nov. 2021. doi: 10.3847/1538-4357/ac1dab.

K. Rajwade, B. Stappers, F. Jankowski, M. Caleb, M. Malenta, V. Morello, M. L. L. Driessen, M. Christiaan Bezuidenhout, and S. Sanidas. Hunting for Fast Radio Bursts with MeerTRAP. In *43rd COSPAR Scientific Assembly. Held 28 January - 4 February*, volume 43, page 1194, Jan. 2021.

V. Ravi et al. A fast radio burst localized to a massive galaxy. *Nature*, 572(7769):352–354, Aug. 2019. doi: 10.1038/s41586-019-1389-7.

J. I. Read, T. Hayfield, and O. Agertz. Resolving mixing in smoothed particle hydrodynamics. *MNRAS*, 405(3):1513–1530, July 2010. doi: 10.1111/j.1365-2966.2010.16577.x.

A. G. Riess et al. Type Ia Supernova Discoveries at z >1 from the Hubble Space Telescope: Evidence for Past Deceleration and Constraints on Dark Energy Evolution. *ApJ*, 607(2):665–687, June 2004. doi: 10.1086/383612.

B. W. Ritchie and P. A. Thomas. Multiphase smoothed-particle hydrodynamics. *MNRAS*, 323(3):743–756, May 2001. doi: 10.1046/j.1365-8711.2001.04268.x.

Y. M. Rosas-Guevara, R. G. Bower, J. Schaye, M. Furlong, C. S. Frenk, C. M. Booth, R. A. Crain, C. Dalla Vecchia, M. Schaller, and T. Theuns. The impact of angular momentum on black hole accretion rates in simulations of galaxy formation. *MNRAS*, 454(1):1038–1057, Nov. 2015. doi: 10.1093/mnras/stv2056.

M. Schaller, C. Dalla Vecchia, J. Schaye, R. G. Bower, T. Theuns, R. A. Crain, M. Furlong, and I. G. McCarthy. The EAGLE simulations of galaxy formation: the importance of the hydrodynamics scheme. *MNRAS*, 454(3):2277–2291, Dec.

2015. doi: 10.1093/mnras/stv2169.

J. Schaye and C. Dalla Vecchia. On the relation between the Schmidt and Kennicutt-Schmidt star formation laws and its implications for numerical simulations. *MNRAS*, 383(3):1210–1222, Jan. 2008. doi: 10.1111/j.1365-2966.2007.12639.x.

J. Schaye, T. Theuns, M. Rauch, G. Efstathiou, and W. L. W. Sargent. The thermal history of the intergalactic medium*. *MNRAS*, 318(3):817–826, Nov. 2000. doi: 10.1046/j.1365-8711.2000.03815.x.

J. Schaye et al. The EAGLE project: simulating the evolution and assembly of galaxies and their environments. *MNRAS*, 446(1):521–554, Jan. 2015. doi: 10.1093/mnras/stu2058.

J. M. Shull, B. D. Smith, and C. W. Danforth. The Baryon Census in a Multiphase Intergalactic Medium: 30% of the Baryons May Still be Missing. *ApJ*, 759(1):23, Nov. 2012. doi: 10.1088/0004-637X/759/1/23.

V. Springel. The cosmological simulation code GADGET-2. *MNRAS*, 364(4):1105–1134, Dec. 2005. doi: 10.1111/j.1365-2966.2005.09655.x.

V. Springel, S. D. M. White, G. Tormen, and G. Kauffmann. Populating a cluster of galaxies - I. Results at [formmu2]z=0. *MNRAS*, 328(3):726–750, Dec. 2001a. doi: 10.1046/j.1365-8711.2001.04912.x.

V. Springel, N. Yoshida, and S. D. M. White. GADGET: a code for collisionless and gasdynamical cosmological simulations. *New Astronomy*, 6(2):79–117, Apr. 2001b. doi: 10.1016/S1384-1076(01)00042-2.

V. Springel, T. Di Matteo, and L. Hernquist. Modelling feedback from stars and black holes in galaxy mergers. *MNRAS*, 361(3):776–794, Aug. 2005. doi: 10.1111/j.1365-2966.2005.09238.x.

H. Tanimura, G. Hinshaw, I. G. McCarthy, L. Van Waerbeke, N. Aghanim, Y.-Z. Ma, A. Mead, A. Hojjati, and T. Tröster. A search for warm/hot gas filaments between pairs of SDSS Luminous Red Galaxies. *MNRAS*, 483(1):223–234, Feb. 2019. doi: 10.1093/mnras/sty3118.

H. Tanimura, N. Aghanim, A. Kolodzig, M. Douspis, and N. Malavasi. First detection of stacked X-ray emission from cosmic web filaments. *A&A*, 643:L2, Nov. 2020. doi: 10.1051/0004-6361/202038521.

S. P. Tendulkar et al. The Host Galaxy and Redshift of the Repeating Fast Radio

Burst FRB 121102. *ApJL*, 834(2):L7, Jan. 2017. doi: 10.3847/2041-8213/834/2/L7.

S. D. M. White. Formation and Evolution of Galaxies: Les Houches Lectures. astro-ph/9410043, 1994.

R. P. C. Wiersma, J. Schaye, and B. D. Smith. The effect of photoionization on the cooling rates of enriched, astrophysical plasmas. *MNRAS*, 393(1):99–107, Feb. 2009a. doi: 10.1111/j.1365-2966.2008.14191.x.

R. P. C. Wiersma, J. Schaye, T. Theuns, C. Dalla Vecchia, and L. Tornatore. Chemical enrichment in cosmological, smoothed particle hydrodynamics simulations. *MNRAS*, 399(2):574–600, Oct. 2009b. doi: 10.1111/j.1365-2966.2009.15331.x.

J. M. Yao, R. N. Manchester, and N. Wang. A New Electron-density Model for Estimation of Pulsar and FRB Distances. *ApJ*, 835(1):29, Jan. 2017. doi: 10.3847/1538-4357/835/1/29.

Y. B. Zel'dovich. Reprint of 1970A&A.....5...84Z. Gravitational instability: an approximate theory for large density perturbations. *A&A*, 500:13–18, Mar. 1970.

B. Zhang. Fast Radio Burst Energetics and Detectability from High Redshifts. *ApJL*, 867(2):L21, Nov. 2018. doi: https://doi.org/10.3847/2041-8213/aae8e3.

Z. J. Zhang, K. Yan, C. M. Li, G. Q. Zhang, and F. Y. Wang. Intergalactic Medium Dispersion Measures of Fast Radio Bursts Estimated from IllustrisTNG Simulation and Their Cosmological Applications. *ApJ*, 906(1):49, Jan. 2021. doi: 10.3847/1538-4357/abceb9.

The End